10

Metallurgy, Processing and Reliability of Lead-Free Solder Joint Interconnections

Jin Liang[a], Nader Dariavach[a], and Dongkai Shangguan[b]

[a]*EMC Corp., Hopkinton, MA 01748, USA*
[b]*FLEXTRONICS, San Jose, CA 95131, USA*

10.1. INTRODUCTION

Soldering is one of the most important manufacturing processes in the electronics industry. Reliable, high quality, long-lasting electronic products demand uncompromised integrity of each individual solder interconnection inside electronic packages and in PCB/component assemblies. The drive to lead-free soldering due to global legislations and market forces has a fundamental effect on material selection and manufacturing processes in the industry. The current viable Pb-free solders are based on the near-eutectic composition of the Sn-Ag-Cu ternary system with or without additions of other alloying elements. These Pb-free alloys have higher melting temperatures, different mechanical and physical properties from the current Sn-Pb eutectic solders, and could have significant implications in terms of soldering processes, compatibility, and end product reliability.

In this chapter, the metallurgy, processing and reliability of lead-free solder joint interconnections is discussed. Intermetallic formation kinetics and morphology, as well as microstructures of typical lead-free solder joints, are presented, followed by a discussion on the solder wetting behavior with different board and component metallic finishes and general process compatibility with the current technologies of packaging, design, and processing. Furthermore, this chapter reviews effects of mechanical loading and thermal conditions on the time-dependent non-linear deformation and fatigue behavior of lead-free solder alloys. An attempt is made to compare the reliability of Pb-free solder joint interconnections to the Sn-Pb eutectic solder joints in different applications and loading conditions. A guideline is provided at the end of this chapter for better utilization of the unique beneficial attributes of Pb-free alloys, and for prevention of potential processing and reliability issues.

10.2. PHYSICAL METALLURGY OF LEAD-FREE SOLDER ALLOYS

Use of lead-bearing solders, such as the Sn-Pb eutectic solder, can be dated back to early human history. In the last 50 years, the Sn-Pb solders have found extensive usage in electronic and semiconductor industries for large volume production for printed circuit board (PCB)/component assemblies with highly automated processes and process controls. In principle, solders are used for joining purposes because they possess the following useful characteristics: a liquidus temperature lower than melting points of the materials to be joined; molten solders wet or spread on the substrate metallic or metalization surfaces and form sound metallic bonds without significant erosion of the surfaces to be joined [1]. Strengths of the final solder interconnections are determined by the solder chemical composition, processing conditions, and particularly by the metallurgical reactions of the molten solder with the metallic surfaces to be joined. The interfacial reactions, such as wetting or spreading between molten solder and metallic surfaces, depend on many factors, such as intrinsic chemical affinity, surface cleanness, thermodynamics and kinetics of intermetallic formation and growth.

10.2.1. Tin-Lead Solders

The Sn-Pb binary system has a eutectic reaction around 183°C with a composition of 63Sn-37Pb (wt%). The eutectic reaction is taken as the following form [2,3]:

$$\mathrm{L} \rightarrow \beta \text{ Sn (solid solution with Pb, tetragonal lattice)} + \alpha \text{ Pb (solid solution with Sn, BCC lattice).}$$

The solubility at the eutectic temperature is 19% of Sn in Pb, and 2.5% of Pb in Sn. The Sn solubility in Pb decreases significantly to less than 2% at room temperature, while Pb solubility in Sn is reduced to literally zero. Thus, during the solidification or aging at room temperature, the secondary Pb and Sn will precipitate from the original Sn-Pb eutectic structures. Also, Sn-Pb solders with compositions other than eutectic will also have primary lead phase (for Pb-rich solders) or primary Tin-rich phase (for Tin-rich solders) forms as dendrites, with subsequent precipitations of saturated Pb or Tin phases within these primary phases.

The Sn-Pb solder alloys offer the following advantages as compared with other solders:

(1) Superior wetting and spreading characteristics on metallic substrates, such as, Au, Pt, Pd, Cu, Ni, Ag, and other metals and alloys, with minimal substrate erosion.
(2) Satisfactory metallic bonding strength, ductility, stiffness, and fatigue resistance.
(3) Ready application as soldering preservation coatings on PCBs and on component leads by electro-plating or dipping.
(4) Relatively inexpensive to produce and use.

However, lead (Pb), as a pure element or an additive and alloying element, is also toxic to human beings. For this reason it has been or will be banned for use in many industries and applications. Even with its superior manufacturing process attributes in the electronics industry, the European Union has passed laws to ban the usage of Pb in electronic products starting from July 1, 2006 [4,5].

10.2.2. Lead-Free Solder Alloys

For a smooth transition to lead-free soldering, ideally, the lead-free alloys would have melting points around 180°C, close to that of the Sn-Pb eutectic alloy, and are of their constituent eutectic compositions. However, there are very few tin-based Pb-free solder alloys that satisfy the above criteria. Sn-Bi (42Sn-58Bi) eutectic and Sn-In (48Sn-52In) eutectic have relatively low melting points, 138°C and 118°C, respectively [6,7]. Due to relative poor high temperature mechanical strength, lack of ductility (for Sn-Bi alloys), and limited resource, these alloys are finding only very limited applications in the industry. Sn-Zn or Sn-Zn-Bi alloys have melting points close to the Pb-Sn eutectic alloys, and have been used with some success, particularly in East Asia for some consumer products [8]. However, with Zinc being prone to oxidation in the high temperature soldering processes, and to corrosion (possible conductive corrosion by-products), these alloys are unlikely to be used for volume production as a general Pb-free solution. The currently most promising Pb-free solder candidates are based on the Sn-Ag-Cu ternary system, which has a eutectic composition around Sn-3.8Ag-0.7Cu, melting temperature around 217°C, about 34°C above that of the Sn-Pb eutectic alloy (183°C) [9].

The potential Pb-free candidates are listed in Table 10.1 and shown in Figure 10.1. Both eutectic composition and non-eutectic alloys are shown. For increased fluidity of molten solders, non-eutectic alloy's paste range (the temperature range from solidus to liquidus points) should be kept as small as possible.

The binary system phase diagrams for Sn-Ag and Sn-Cu are shown in Figure 10.2 and Figure 10.3, respectively [10,11]. Unlike Sn-Pb eutectic alloy, the Sn-Cu and Sn-Ag alloys form eutectic reactions with their intermetallic compounds (η' Cu_6Sn_5 for the Sn-Cu binary system and γ Ag_3Sn for the Sn-Ag system) instead of their solid solutions like in the case of the Sn-Pb binary system. Under a nearly thermodynamic equilibrium solidification condition, tin will solidify as nearly pure β phase without any significant solid solution of either Ag or Cu, co-existing with η' Cu_6Sn_5 for the Sn-Cu system or γ Ag_3Sn for the Sn-Ag system. However, under most industrial solidification conditions, the eutectic reactions will be off-equilibrium, thus beta tin could contain solid solute atoms of Ag and/or Cu.

TABLE 10.1.
Tin-based Pb-free solder alloys [10].

Alloy system	Composition (wt%)	Melting points or range (°C)
Sn-Bi	Sn-58Bi	138 (e)
Sn-In	Sn-52In	118 (e)
	Sn-50In	118–125
Sn-Zn	Sn-9Zn	198.5 (e)
Sn-Bi-Zn	Sn-8Zn-3Bi	189–199
Sn-Cu	Sn-0.7Cu	227 (e)
Sn-Ag	Sn-3.5Ag	221 (e)
	Sn-2Ag	221–226
Sn-Ag-Bi	Sn-3.5Ag-3Bi	206–213
	Sn-7.5Bi-2Ag	207–212
Sn-Ag-Cu	Sn-3.8Ag-0.7Cu	217(e)
	Sn-3.0Ag-0.5Cu	218
Sn-Ag-Cu-Sb	Sn-2Ag-0.8Cu-0.5Sb	216–222
Sn-Sb	Sn-5Sb	232–240
Sn-Au	Au-20Sn	280

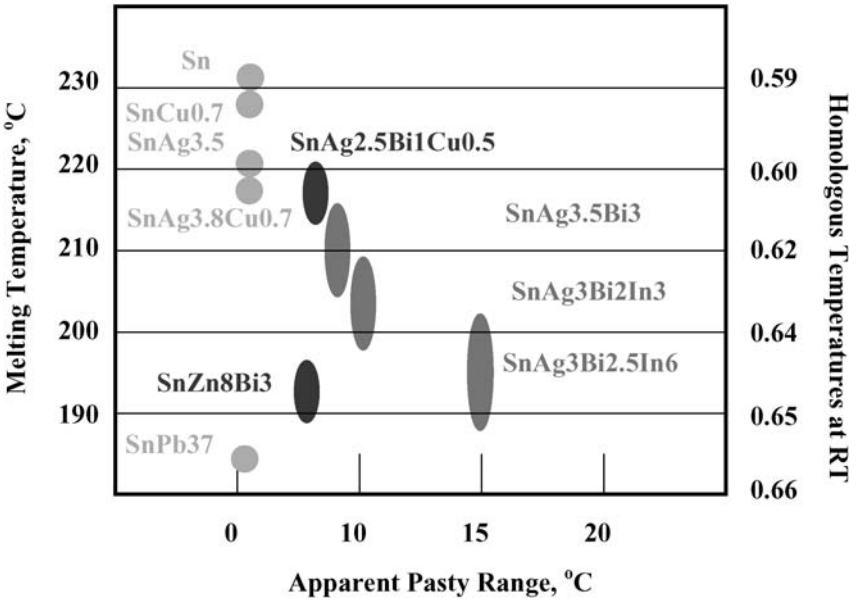

FIGURE 10.1. Pb-free solder candidates to replace the Sn-Pb eutectic solder, their melting temperatures, solidification paste ranges, and homologous temperatures at ambient.

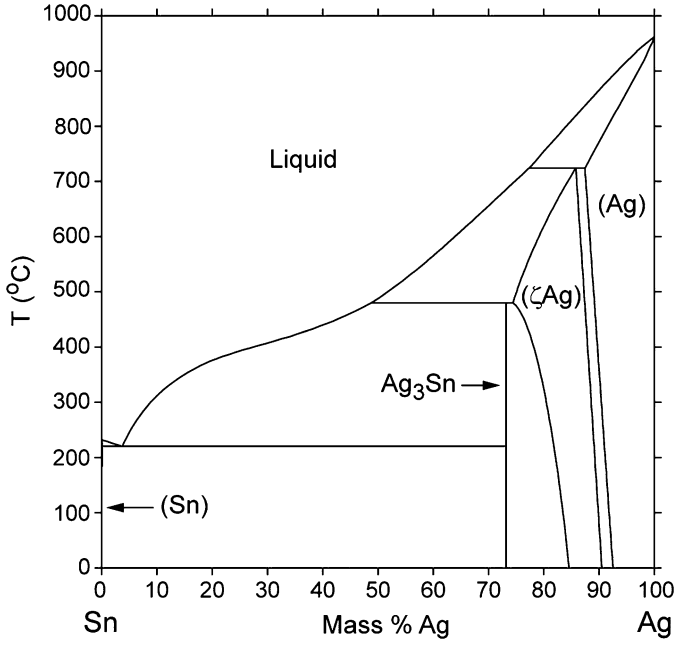

FIGURE 10.2. Sn-Ag binary phase diagram [10].

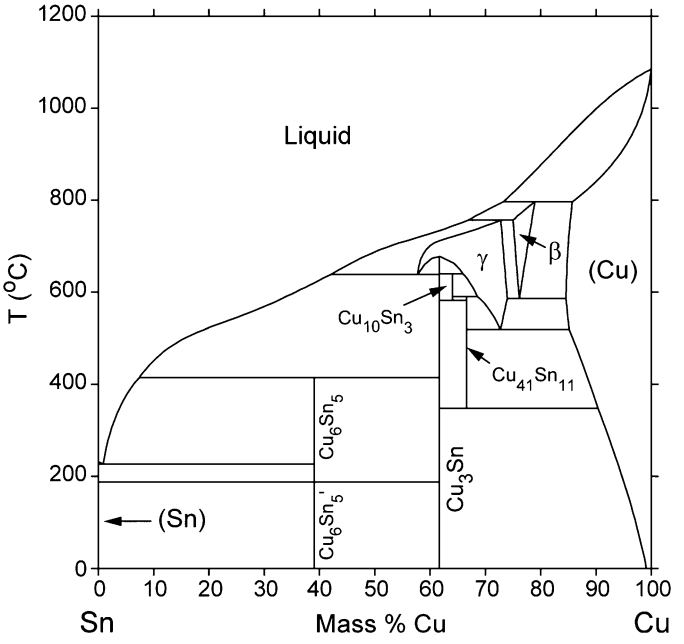

FIGURE 10.3. Sn-Cu binary phase diagram [11].

Subsequent precipitations of stable or metastable intermetallic phases are possible at room temperature and during solidification or aging at temperatures below melting points.

There is still no general agreement about the exact eutectic composition for the Sn-Ag-Cu ternary system; the most reported eutectic compositions are Sn-3.8Ag-0.7Cu and Sn-3.6Ag-0.9Cu (wt%). Currently, the most widely recommended and studied Pb-free alloys are SAC387 (Sn-3.8Ag-0.7Cu) and SAC305 (Sn-3.0Ag-0.5Cu), along with SAC369 (Sn-3.9Ag-0.6Cu) and SAC405 (Sn-4.0Ag-0.5Cu), and a handful of quaternary systems, such as Sn-Ag-Cu-Bi and Sn-Ag-Cu-Fe [12].

The ternary eutectic reaction of the Sn-Ag-Cu system can be expressed as [13]:

$$\mathrm{L} \rightarrow \mathrm{Ag_3Sn} + \mathrm{Cu_6Sn_5} + \beta\ (\mathrm{Sn}).$$

Depending on the exact chemical compositions and solidification conditions (cooling rates, undercooling temperature ranges, etc.), Sn-Ag-Cu alloys may experience primary reactions prior to the ternary eutectic reaction. For example, it was reported that for SAC387, the solidification reaction sequence was found to be [13]:

$$\mathrm{L} \rightarrow \mathrm{L1} + \mathrm{Ag_3Sn} \text{ at } 221.9^{\circ}\mathrm{C},$$

$$\mathrm{L1} \rightarrow \mathrm{L2} + \beta\ (\mathrm{Sn}) \text{ at } 218.7^{\circ}\mathrm{C},$$

$$\mathrm{L2} \rightarrow \mathrm{Ag_3Sn} + \mathrm{Cu_6Sn_5} + \beta\ (\mathrm{Sn}) \text{ at } 217^{\circ}\mathrm{C}.$$

However, should the Ag concentration be less than the eutectic composition, the first reaction would not take place. The possible exiting phases in the Sn-Ag-Cu ternary system are

TABLE 10.2.
Phases, crystal structures in Sn-Ag-Cu system [10].

Phase	Common names	Spacegroup	Chemical composition
Liquid	L	n/a	$(Ag,Cu,Sn)_1$
FCC	(Ag), (Cu)	Fm-3m	$(Ag,Cu,Sn)_1(Va)_1$
BCC	(beta Cu), beta	Im-3m	$(Cu,Sn)_1(Va)_3$
HCP	(zeta Ag), (epsilon Pb)	$P6_3/mmc$	$(Ag,Sn)_1(Va)_{0.5}$
BCT	(Sn), (beta Sn)	$I4_1/amd$	$(Ag,Cu,Sn)_1$
Ag_3Sn	epsilon	Pmmn	$(Ag)_{0.75}(Sn)_{0.25}$
$Cu_3Sn.h$	gamma	Fm-3m	$(Cu,Sn)_{0.75}(Cu,Sn)_{0.25}$
$Cu_{41}Sn_{11}$	delta	F-43m	$Cu_{0.788}Sn_{0.212}$
$Cu_{10}Sn_3$	zeta	$P6_3$	$Cu_{0.769}Sn_{0.231}$
Cu_3Sn	epsilon	Cmcm	$Cu_{0.75}Sn_{0.25}$
Cu_6Sn_5	eta, $Cu_6Sn_5.h$	$P6_3/mmc$	$Cu_{0.545}Sn_{0.455}$
Cu_6Sn_5'	eta′, $Cu_6Sn_5.l$	...	$Cu_{0.545}Sn_{0.455}$

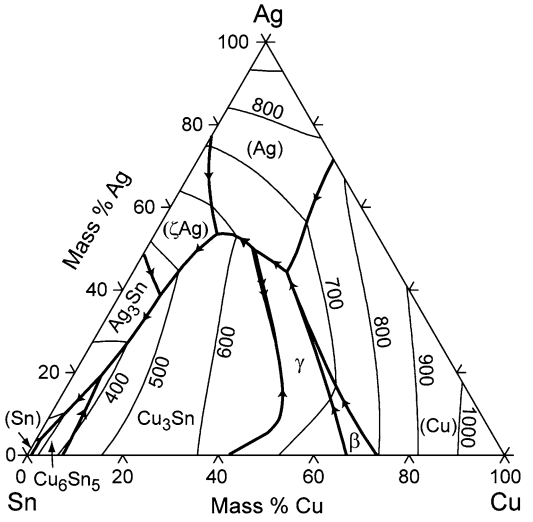

FIGURE 10.4. A projection of Sn-Ag-Cu phase diagram showing the ternary eutectic reaction.

listed in Table 10.2 [14]. The projected ternary phase diagram is shown in Figure 10.4. Figure 10.5 shows the detailed phase-temperature relationships at the Tin-rich corner where most of the current Pb-free solder alloys are based.

The typical Sn-Pb and -Sn-Ag-Cu solidification structures and microstructures are shown in Figure 10.6, with the pictures taken *in-situ* with an ESEM with heating stage [15]. The as-solidified structures for Sn-Ag-Cu (SAC378) and Sn-Pb eutectic have sharp difference. The Sn-Pb eutectic solder solidifies as dendrites and fine eutectic two phase structures. For SAC387, the structure is of fine plate shape without obvious ternary eutectic structure seen with the unpolished surface at low magnification. Also, the SAC alloy tends to have more solidification shrinkage and looks dull compared to the Sn-Pb eutectic solder, which is much smoother and shinier. The microstructures of actual Sn-Ag-Cu solder joints for a chip capacitor and a BGA solder ball are shown in Figure 10.7 and Figure 10.8. High magnification optical micro-photos for Sn-Ag-Cu solder on Ag (Figure 10.9) and OSP (Fig-

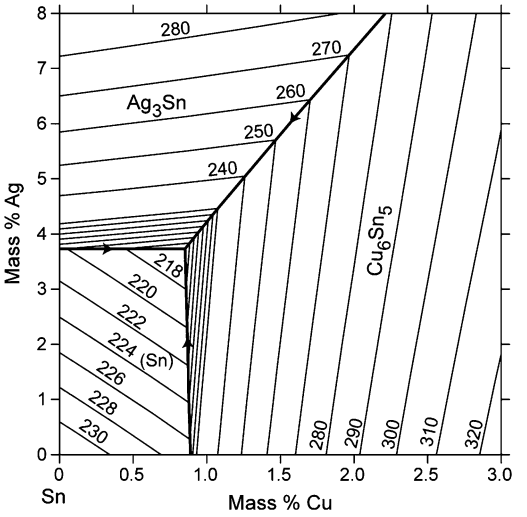

FIGURE 10.5. Sn-Ag-Cu phase diagram at the Sn-rich corner [14].

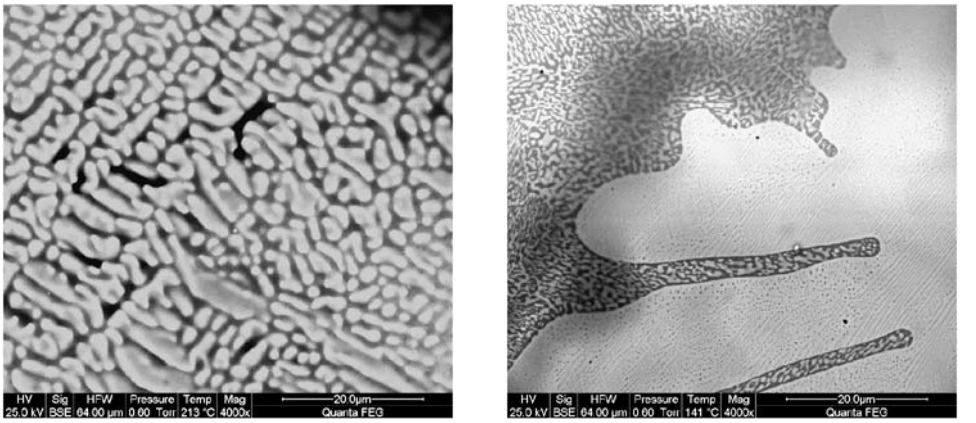

(a) (b)

FIGURE 10.6. Typical as-solidified structures of solders, (a) SAC387 Pb-free; (b) Sn-Pb eutectic.

ure 10.10) finish boards show clearly secondary intermetallic phases present in the SAC378 alloy, and a bilayer of intermetallic compounds at the solder-Cu substrate interface.

10.2.3. Interfacial Reaction: Wetting and Spreading

The wetting of a molten solder on metallic surfaces is a rather complex phenomenon. The soldering technology has generally evolved in an empirical manner. Factors, such as the conditions of the metallic surfaces (i.e., the nature of oxides or other films, surface roughness), temperature distribution during the soldering, as well as the interfacial metallurgical reactions, and flux chemical reaction with the metallic surface, all play important roles in determining the final solder wetting, spreading and the solder joint shape, as well as the mechanical strength of the joints in general [1].

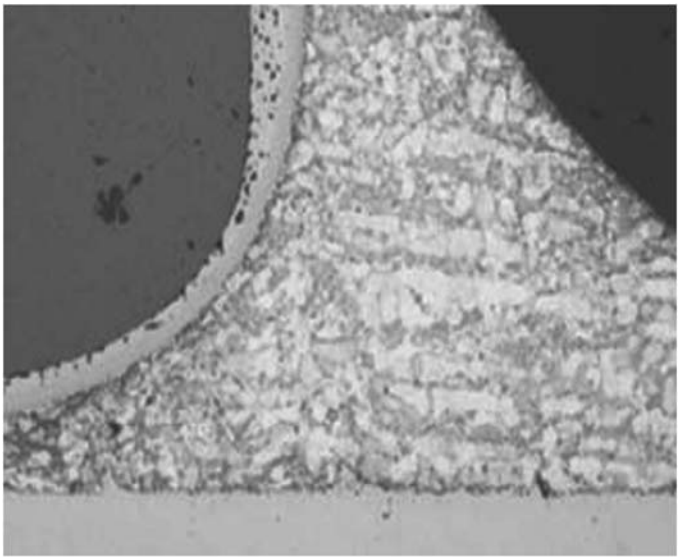

FIGURE 10.7. Microstructure of Sn-Ag-Cu solder joint for a chip capacitor.

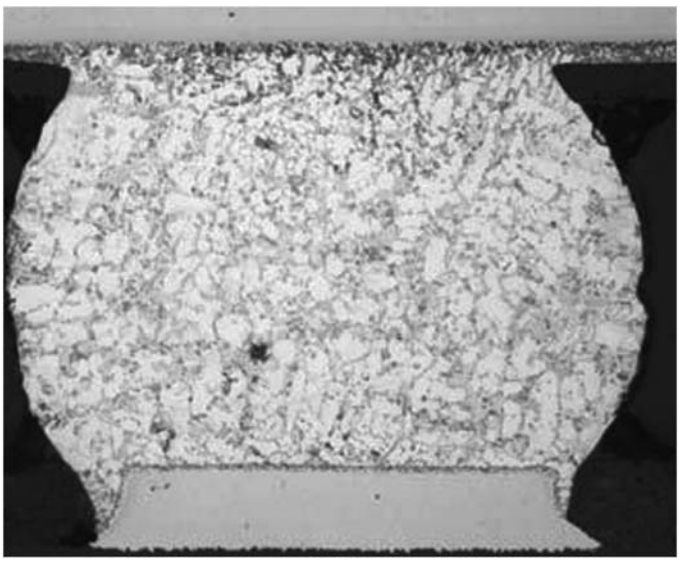

FIGURE 10.8. Microstructure of Sn-Ag-Cu solder for a BGA solder ball.

Classic wetting theory has been established on simple systems like water or oil on a non-reaction surface, such as glass, at relatively low temperatures. The physico-absorption-dominated wetting driving force is the capillary reaction to reduce the total surface energy in the liquid-solid-vapor system of interest. The restraining force for the wetting or spreading is viscosity. At balance, the three surface tensions between the liquid/solid substrate

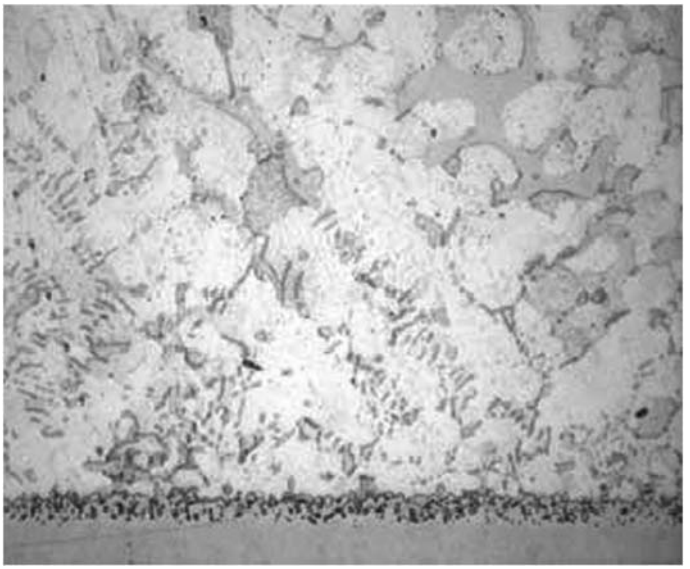

FIGURE 10.9. Microstructure of Sn-Ag-Cu solder on Ag finish board.

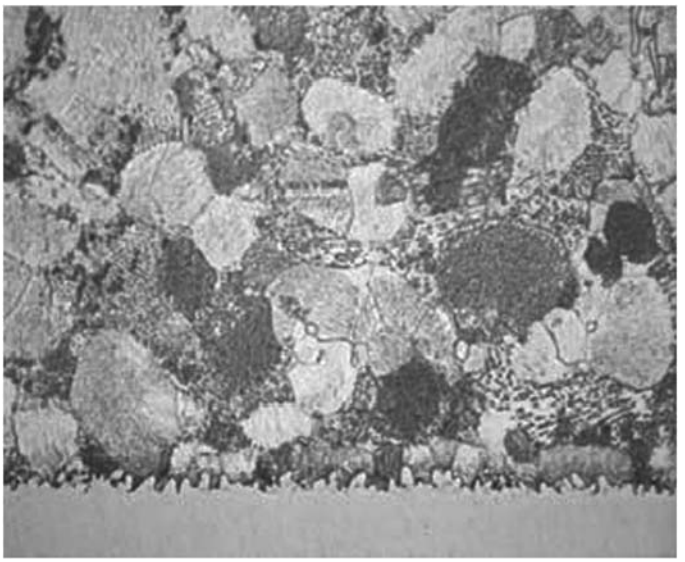

FIGURE 10.10. Microstructure of Sn-Ag-Cu solder on OSP finish board.

(γ_{LS}), the liquid/vapor (γ_{LV}), and the solid substrate/vapor (γ_{SV}), together determine the final wetting angle θ, which can be expressed as follows [1]:

$$\cos\theta = \frac{\gamma_{SV} - \gamma_{LS}}{\gamma_{LV}}. \tag{10.1}$$

A perfect wetting means that the wetting angle θ approaches zero. For physical wetting, the efficient way to decrease the wetting angle is to increase the surface energy of solid substrate/vapor (γ_{SV}) by cleaning the solid surface with removal of absorbed species which tend to reduce the surface energy of the solid surface. The surface energy between the liquid/solid substrate (γ_{LS}), is constant for a given non-reaction solid–liquid system, but very much temperature dependent. As temperature rises, γ_{LS} decreases rapidly, thus promoting wetting and spreading of the liquid phase. The liquid/vapor surface energy (γ_{LV}) is also constant under a fixed temperature and pressure condition for a particularly liquid–vapor system. It changes with pressure and atmosphere chemical composition. Lower pressure or vacuum will reduce (γ_{LV}), thus promoting the wetting and spreading.

The soldering process almost invariably involves many physical-chemical reactions at the interfacial and liquid–solid–vapor junction area. The surface tension energies between the liquid/solid substrate (γ_{LS}) and between the solid/vapor substrate (γ_{SV}) are changed rapidly both by flux chemical reactions, dissolution of parent metals, and intermetallic formations at the junction area. The pure physical wetting phenomenon takes place rather quickly (from 100 ns to 10 ms), while wetting or spreading of molten solder takes a much longer time (usually from 0.5 second to up to a few of minutes), indicating the spreading rate and wetting angle in the soldering process are very much dependent on the complex local chemical reaction kinetics and thermodynamics [1], not a purely physical wetting process.

The surface tension energies between the liquid/solid substrate (γ_{LS}) in a solderable system may be significantly different before and after interfacial reactions. The formation of an intermetallic layer would reduce the total energy balance at the liquid-solid interface. Assuming the Gibbs free energy per unit area for forming an intermetallic layer between the molten solder and the metallic substrate is ΔG_r (which is a negative number), the surface energy between the liquid/solid substrate can be expressed as:

$$\gamma_{LS} = \gamma_{LS}^0 + \Delta G_r, \tag{10.2}$$

where γ_{LS}^0 is the surface tension energy between liquid and solid before any interfacial reaction takes place. Since ΔG_r is a negative number, the liquid/solid surface tension energy γ_{LS} is reduced by the formation of the intermetallic layer, thus reducing the wetting angle according to Equation (10.1). Furthermore, it has been found that the absolute ΔG_r value is much larger (by two orders of magnitude) than the initial surface energy for molten solders between the liquid/solid substrate, as reported by Yost and Roming [16] and Wang and Conrad [17]. Therefore, it is clear that anything that affects proper intermetallic formation will cause significant change to the wetting rate and wetting angle in the soldering processes. This explains why molten solders rarely wet or spread on some metallic (such as aluminum and its alloys) and nonmetallic (such as ceramic and plastic) surfaces which do not form an intermetallic layer or the intermetallic formation kinetics is too slow to promote wetting and spreading of the molten solders.

As discussed above, the wetting and spreading of molten solders depend on many factors. Should a clean surface be maintained, typical wetting angles for any liquid solder and metallic substrates are intrinsic wettability compatibility measurements, which are dependent on chemical compositions of the liquid solder and solid substrates. Table 10.3 gives some typical wetting angles for Sn-Pb eutectic solder, and some Sn-based Pb-free alloys on different metallic substrates or metalization surfaces at the typical reflow temperatures for these alloys. What is clear from this table is that the intrinsic wetting angles of

TABLE 10.3.
Typical wetting angles for Sn-based Pb-free alloys [16].

	Reflowed alloy pellet (Sn+)					
Substrate	0.5Cu	3.5Ag	3.8Ag0.7Cu	3.5Ag0.7Cu	3.8Ag0.7Cu0.5Sb	37Pb
Cu	42	43	43	41	43	12
Ag	19	26	24	30	33	13
Sn37Pb	19	19	22	20	22	5
Sn0.7Cu	15	11	18	11	10	17
Au over Ni	9	6	10	14	5	4

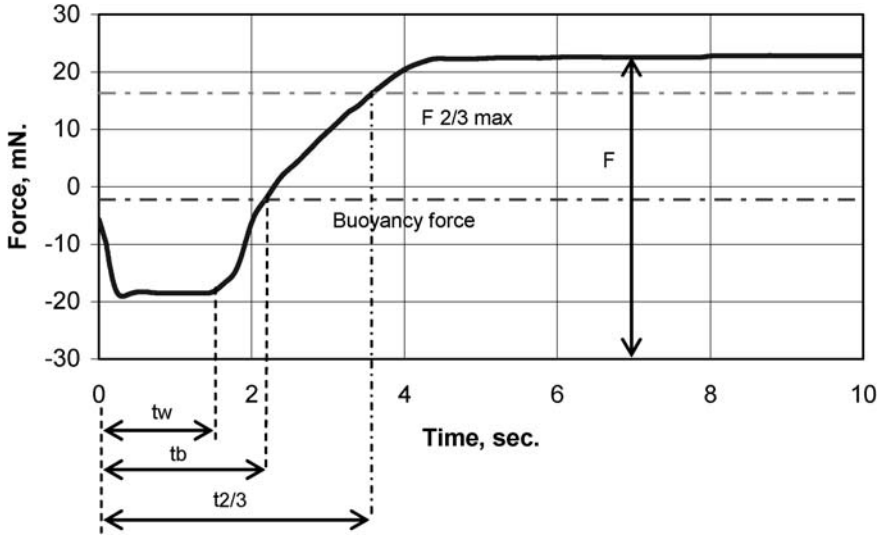

FIGURE 10.11. Wetting balance test interpretation.

Sn-based Pb-free alloys are not as good as those for the 63Sn-37Pb eutectic alloy on the copper substrate and other metallic finishes. However, most Pb-free alloys wet very well on Ni/Au metalization surface; and the wetting angles of these Pb-free alloys on Au/Ni are close or better than that for Sn-Pb eutectic on copper surface.

Another way for wettability evaluation under dynamic conditions is the wetting balance test, which involves investigation of both wetting times and wetting forces [18]. This method uses immersion of test samples into a solder bath, then recording the vertical force, which is the sum of buoyancy and surface tension forces over time. The typical wetting curve is shown in Figure 10.11. Commonly measured wetting balance characteristics are the initial wetting time t_w, the time for the wetting curve to re-cross the buoyancy force line t_b, the maximum wetting force F_{max} and the time required to rich the $2/3$ of the maximum force $t_{2/3}$. The wetting curve comparison for Sn-Pb and three Pb-free alloys, Sn-0.7Cu, Sn-3.5Ag, and Sn-3.8Ag-0.7Cu (SAC387), on copper substrate is shown in Figure 10.12. Measurements were taken at 235°C using $12.5 \times 25.0 \times 0.5$ mm copper test coupons. It can be clearly seen that the wetting times t_w, t_b and $t_{2/3}$ for the Sn-Pb alloy are significantly shorter than those for the Pb-free alloys. The best wetting performance for the tested Pb-free alloys is from the Sn-3.8Ag-0.7Cu alloy. Increasing the test temperature up to 260°C

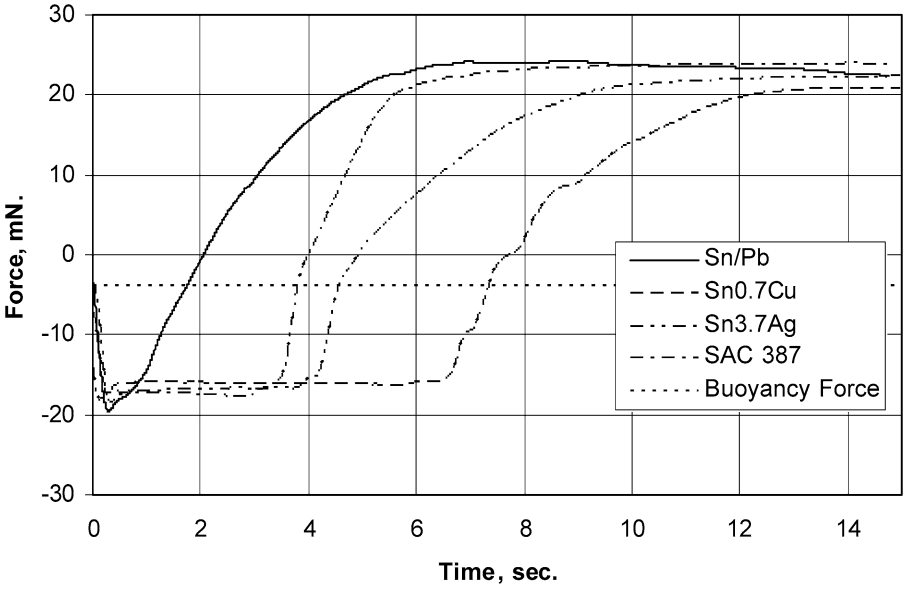

FIGURE 10.12. Wetting balance curves for Sn-Pb eutectic and Pb-free solders at 235°C.

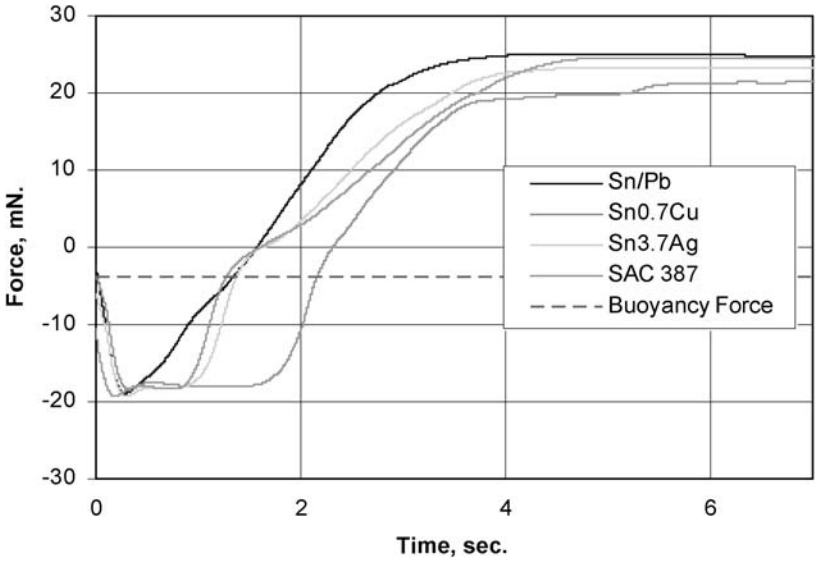

FIGURE 10.13. Comparison of wetting curves at 260°C for Sn-Pb eutectic and Pb-free solders.

decreases the wetting times significantly for these alloys (Figure 10.13). The buoyancy time t_b of Sn-3.5Ag and SAC387 alloys is equal to that of the Sn-Pb alloy at higher temperatures (>250°C). The wetting time t_b of the Sn-0.7Cu alloy is still significantly longer as compared with Sn-Pb eutectic, Sn-3.5Ag and SAC387 at temperatures above 250°C. Figure 10.14 shows the measurement results for initial wetting time at different testing temperatures for all these alloys. From these wetting balance test results, it is clear that the

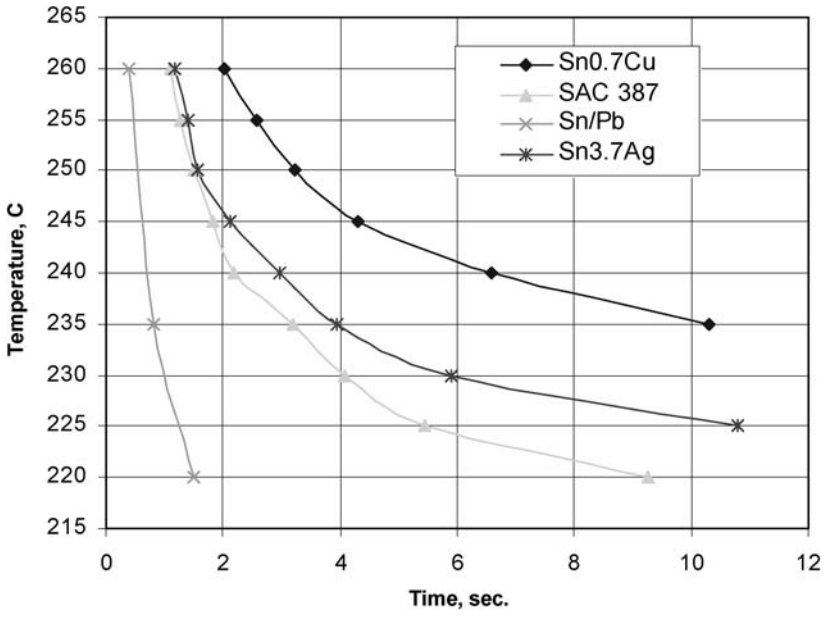

FIGURE 10.14. Comparison of initial wetting time for Sn-Pb eutectic and Pb-free solders.

Pb-free soldering process requires an increase in the process temperature up to 245–250°C for Sn-3.5Ag and Sn-3.8Ag-0.7Cu alloys, and up to 260°C for the Sn-0.7Cu alloy, which has been a candidate Pb-free alloy for wave soldering.

10.2.4. Interfacial Intermetallic Formation and Growth at Liquid–Solid Interfaces

As stated above, the intermetallic growth and substrate dissolution take place rather rapidly during a normal soldering operation. Since lead-free soldering requires substantially higher temperatures (around 250°C), the rates for intermetallic growth and substrate dissolution are expected to be significantly greater for Pb-free solders than those for the current Sn-Pb eutectic solder. A thorough understanding of lead-free solder/substrate interfacial reactions can lead to the optimum lead-free soldering processes and the optimum lead-free coating thicknesses for component and PCB termination finishes. Excessive intermetallic compounds (IMCs) can cause embrittlement of solder joints and decrease fatigue strength, leading to unfavorable reliability for Pb-free PCB assemblies.

10.2.4.1. Intermetallic Growth Kinetics on Cu Substrate Reactions between copper and molten tin at the copper/solder junction for three Pb-free solders, Sn-3.5Ag, Sn-0.9Cu, and Sn-3.8Ag-0.7Cu, produced a bilayer of Cu_6Sn_5 adjacent to the solder and Cu_3Sn adjacent to the copper [19]. Figures 10.15, 10.16 and 10.17 present SEM images of IMC layers formed at 235°C for 10 sec, 3 min, 30 min and 2 hr holding times for these three solders. After holding for 10 sec, thin Cu_6Sn_5 intermetallic layers of average thicknesses of 1.18, 1.33 and 1.24 μm, were observed respectively for the three alloys. The presence of the Cu_3Sn phase for these samples was not detected at this temperature for such a short time. Cu_3Sn phase, however, appears with increased holding time. The final average thicknesses of the IMCs after holding for 2 hrs were 6.97, 7.65 and 9.44 μm for the three solders on copper substrate. The maximum thicknesses for the three alloys were determined to be

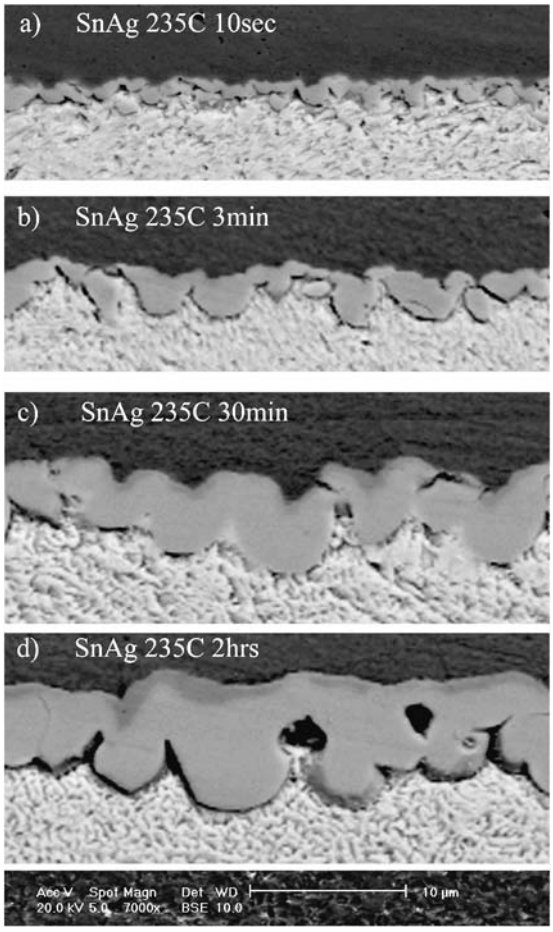

FIGURE 10.15. Comparison of SEM images of the intermetallic layers for the SnAg alloy cast at 235°C and held for 10 sec (a), 3 min (b), 30 min (c), 2 hrs (d).

8.42, 10.37 and 16.5 μm. The similarity of the scalloped intermetallic microstructures for all three alloys indicates that the mechanism of growth is the same for all three. Comparison of the scanning micrographs in Figure 10.17 with those in Figures 10.15 and 10.16 clearly shows that the intermetallic grows faster in the Sn-Ag-Cu (SAC387) alloy than in the other two alloys.

Figure 10.18 illustrates effects of temperature on IMC growth for Sn-3.5Ag alloy at 225 and 280°C. The sample held for 30 sec does not show the presence of Cu_3Sn. Increasing the temperature up to 280°C promotes Cu_3Sn layer formation with a thickness of 0.36 μm. The total average thickness of the IMC increases by 89% from 1.14 μm up to 2.16 μm with an increase in temperature from 225 to 280°C.

The IMC layer growth varies depending on the diffusion rates of Cu and Sn through the Cu_6Sn_5 and Cu_3Sn layers and the reactions at the layer interfaces. It is further complicated by the fact that the Cu_6Sn_5 layer is scalloped [20,21]. As such, the thickening or

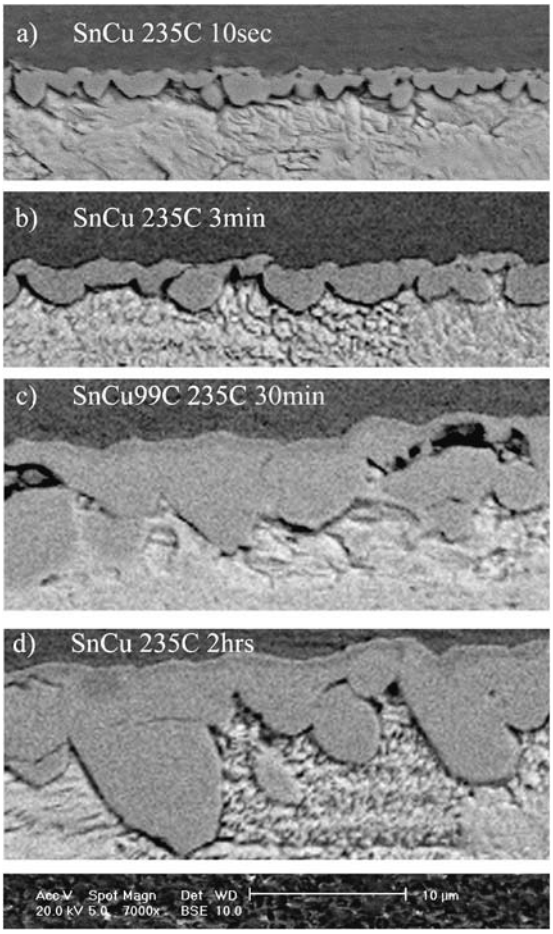

FIGURE 10.16. Comparison of SEM images of the intermetallic layers for the SnCu cast at 235°C and held for 10 sec (a), 3 min (b), 30 min (c) and 2 hrs (d).

growth kinetics of the total IMC layer has been evaluated by simply assuming parabolic growth. That is, it is assumed that the total layer thickness is given by

$$w = w_0 + kt^{\frac{1}{2}}, \tag{10.3}$$

where w is the intermetallic layer thickness, t is the holding time, k is the IMC growth rate constant, and w_0 is the initial thickness of the IMC layer formed on immersion of the copper sample in the solder bath. As such, the measured average layer thicknesses are plotted as a function of the square root of holding time for each temperature studied and fitted with a linear least squares curve to determine the values of k and w_0 for each temperature. The k values are subsequently analyzed to determine the apparent activation energy (Q) for IMC growth using the Arrhenius equation,

$$k = k_0 e^{-\frac{Q}{RT}} \tag{10.4}$$

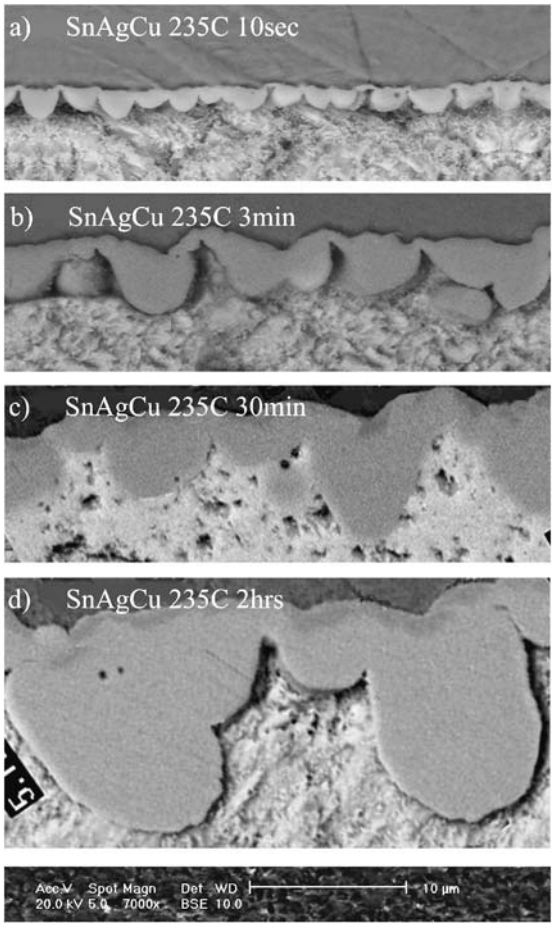

FIGURE 10.17. Comparison of SEM images of the intermetallic layers for the SnAgCu alloy cast at 235°C and held for 10 sec (a), 3 min (b), 30 min (c), 2 hrs (d).

where k_0 is the proportionality constant, Q is the apparent activation energy for IMC layer growth, R is the Boltzmann's constant, and T is the absolute temperature. The apparent activation energy Q was obtained from plots of $\ln(k)$ versus $1/T$.

Figure 10.19 shows the experimental data for IMC layer growth for the SnAgCu (SAC387) alloy as a function of the square root of the holding time for five different temperatures. The linear least squares lines show very good fit to the data, with the average deviation from the experimental data being in the range of $\pm 5\%$. The upper and lower limits of the error bars for the thickness measurements for each time represents the thickness of the biggest scallop and the deepest cusp between scallops, respectively. As can be seen, the minimum and maximum IMC thickness can deviate up to $\pm 75\%$ from the average IMC thickness values calculated from the integration of IMC areas. This difference in IMC thickness can clearly be seen in the SEM images (Figures 10.15–10.18).

Comparison of IMC growth for the SnAg (Sn-3.5Ag), SnCu (Sn-0.9Cu) and SnAgCu (SAC387) lead-free solder alloys at five different temperatures are presented in Figure 10.20. Growth rate constant (k) values obtained from the slopes of the lines fitted to

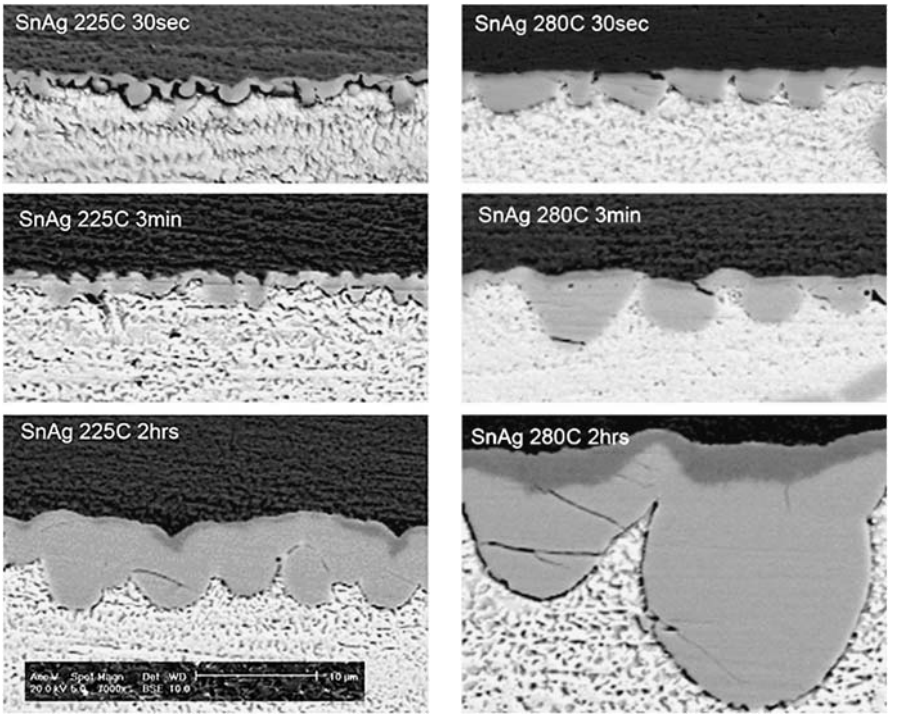

FIGURE 10.18. The IMC thickness comparison for the SnAg alloy cast at 225 and 280°C and held for 30 sec, 3 min and 2 hrs.

TABLE 10.4.
Calculated IMC parabolic growth rates and intercepts for SAC387, Sn3.5Ag and Sn0.7Cu alloys.

	IMC growth rate constant k (μm/sec)		
Temperature, °C	SAC387	Sn3.5Ag	Sn0.7Cu
225	0.096	0.068	–*
235	0.096	0.071	0.077
245	0.120	0.088	0.088
260	0.129	0.094	0.104
280	0.137	0.135	0.122

*225°C testing temperature is below the melting point for Sn0.7Cu alloy.

the data are presented in Table 10.4. It can be seen that IMC growth rate constants for the SnAg and SnCu solder alloys are very similar for all test temperatures, while those for the SnAgCu alloy are about 30% greater. This is consistent with the growth rates being greater for the SnAgCu alloy.

10.2.4.2. Activation Energy and Temperature Effects on Intermetallic Growth on Cu Substrate Comparisons of intermetallic growth for the SnAg, SnCu and SnAgCu alloys at different temperatures are presented in Figures 10.21 and 10.22. As can be seen in Figure 10.21(a), the IMC for the SnAg alloy is thinner than that for the SnAgCu alloy for

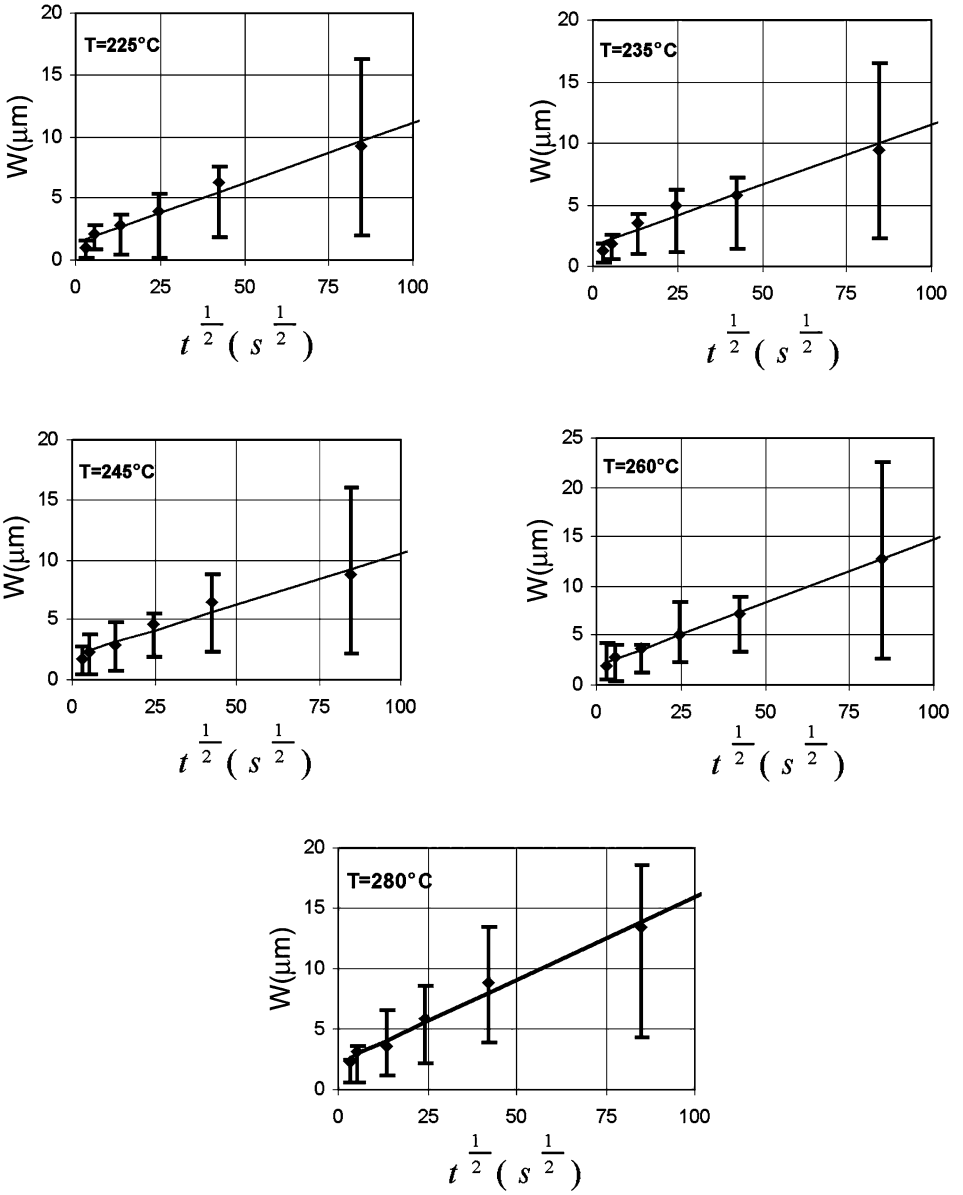

FIGURE 10.19. IMC thickness w as function of the square root of time t for the SnAgCu solder at 225, 235, 245, 260 and 280°C. The straight lines represent mean least square fits of the data.

all exposures. This may result from the SnAgCu alloy being closer to copper saturation at the start of intermetallic growth. It has previously been shown that Cu_6Sn_5/Cu_3Sn intermetallic layer growth for eutectic SnPb solders on copper substrates is slower for growth into solder initially containing no copper than for growth into solder initially saturated with copper. Based on previous studies of copper dissolution into molten eutectic SnAg solder, it is expected that saturation of the copper free solder in this study should require about 60 minutes saturating at 225°C [21].

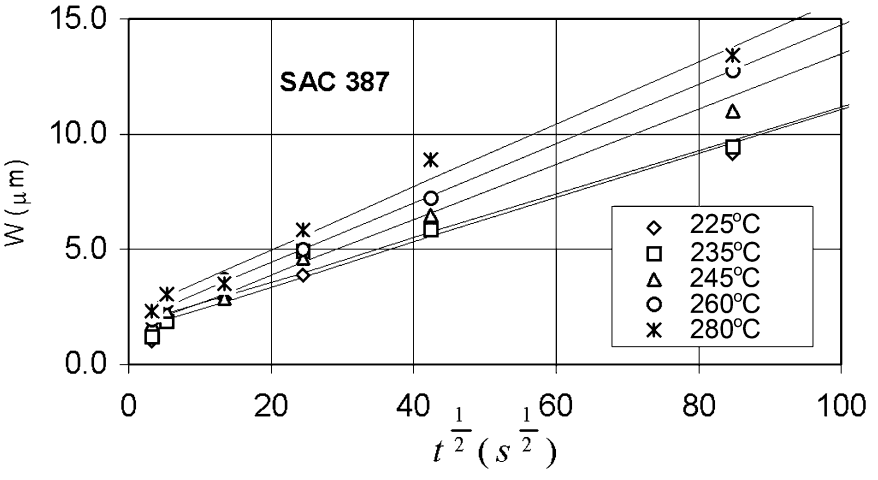

(a)

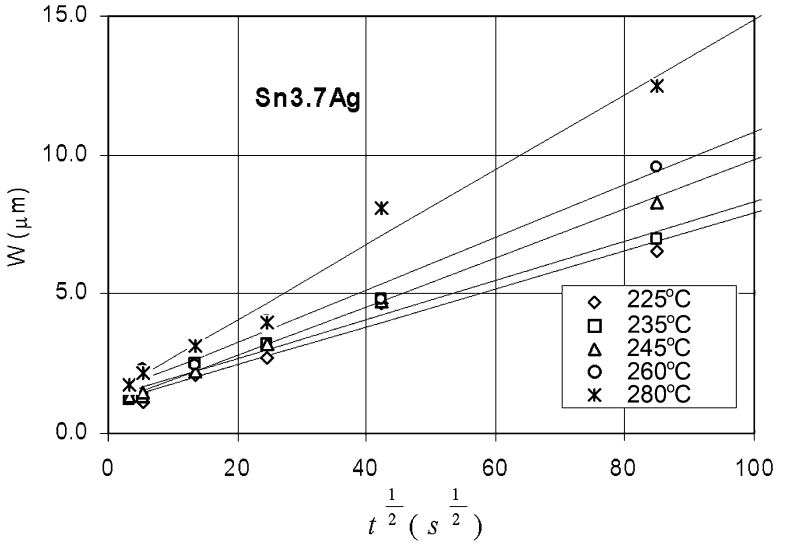

(b)

FIGURE 10.20. IMC growth in copper samples for the SnAgCu (a), SnAg (b) and SnCu (c) lead free alloys as function of the square root of time. Markers represent experimental data and solid lines represent calculated regression data.

As can be seen in Figure 10.21(b) with soldering at 235°C the IMC layers for the SnAgCu alloy again grows faster than the IMC layer for the SnAg alloy. Further, the SnCu alloy, which is molten at this temperature, grows IMC at about the same rate as the SnAg alloy. Figure 10.22(a) and Figure 10.22(b) show a continuation of this trend at 260 and 280°C, with the difference between the IMC growth rates for the SnAgCu solders and the SnAg and SnCu solders being the smallest at 280°C. One reason for this latter effect may be that, as the temperature increases, the solubility of copper in the molten solders increases. Thus, the presence of copper in the SnAgCu alloy is further from the saturation level and IMC growth in all of the solders is characteristic of growth into a solder with relatively low

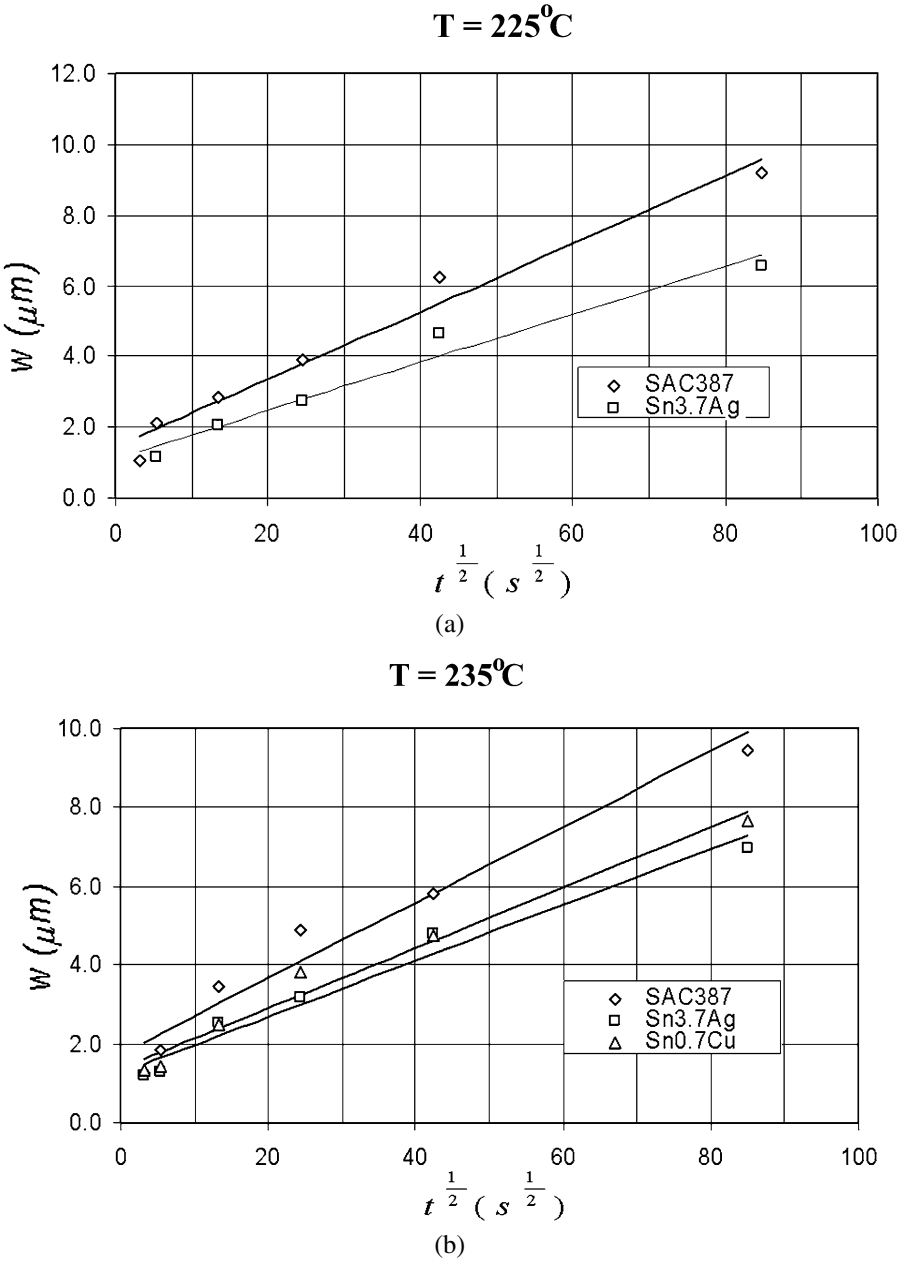

FIGURE 10.21. IMC thickness as function of the square root time for 225°C (a) and 235°C (b). Solid lines represent a calculated fit through the experimental data.

copper content. Following this reasoning, the IMC growth rates for all three solders studied should approach each other as the soldering temperature increases.

Arrhenius plots of the IMC growth constant values given in Table 10.4 are presented in Figure 10.23 and the apparent activation energies are given in Table 10.5. As can be seen, the apparent activation energy for intermetallic growth in the SnAgCu alloy is lower than

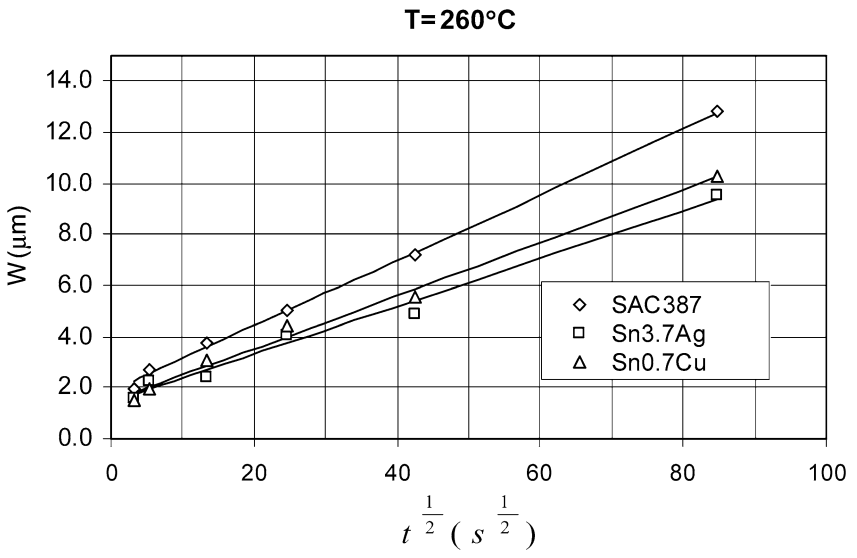

(a)

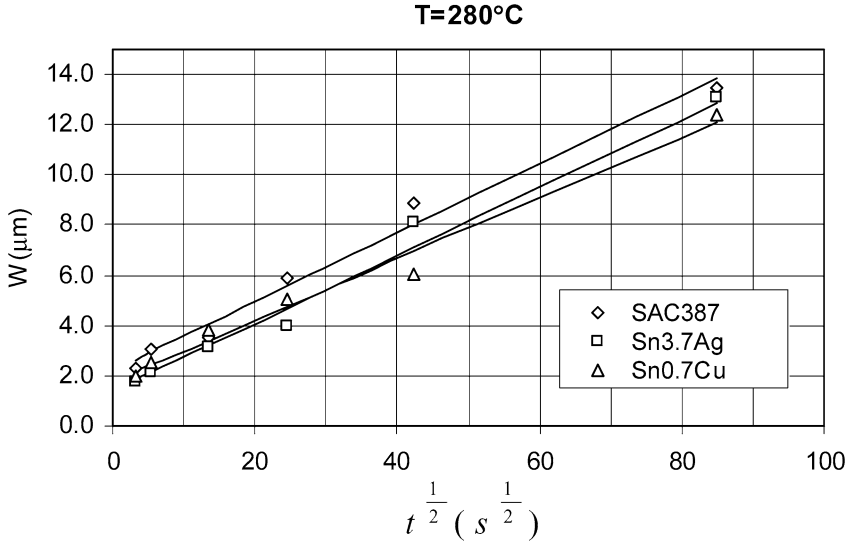

(b)

FIGURE 10.22. IMC thickness as function of the square root of time for 260°C (a) and 280°C (b). Solid lines represent a calculated fit through the experimental data.

TABLE 10.5.
Calculated activation energy for IMC growth of SAC387, Sn3.5Ag and Sn0.7Cu lead free alloys.

Alloy	Activation energy Q, kcal/mol
SAC387	16.44
Sn3.5Ag	25.74
Sn0.7Cu	23.71

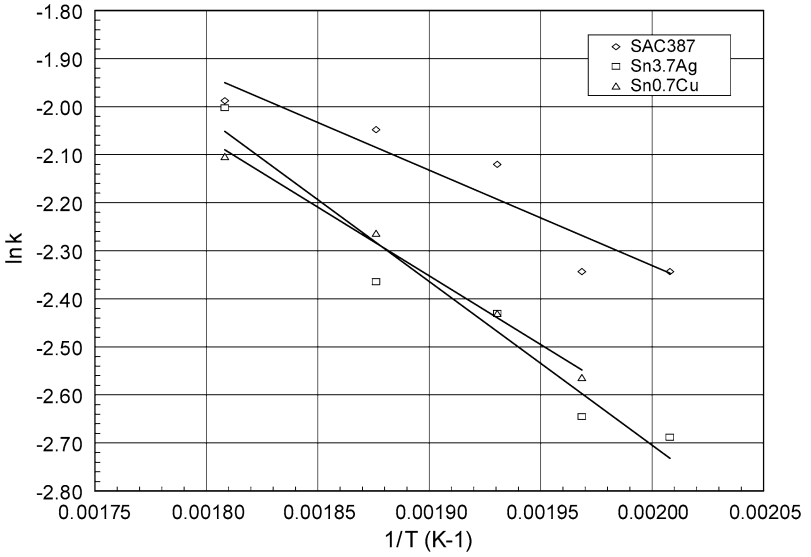

FIGURE 10.23. Arrhenius plot of IMC growth constants (k).

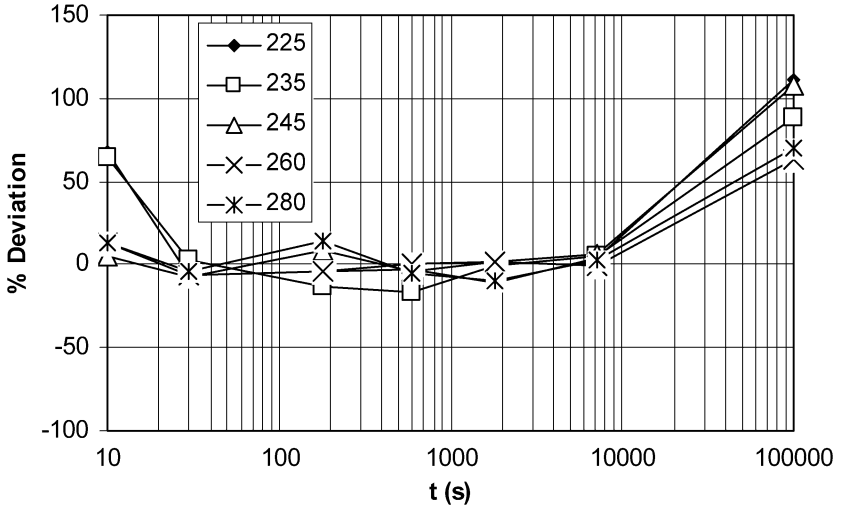

FIGURE 10.24. Deviation of the linear least squares fit values of IMC thickness from experimental data for the SnAgCu alloy at 225, 235, 245, 260 and 260°C.

that for the SnAg and SnCu alloys. This is consistent with the growth rates for this alloy being faster. The values for the SnAg and SnCu alloys are consistent with those reported previously for IMC layer growth for eutectic Sn-Ag solder [22,23].

10.2.4.3. Initial Stage of Intermetallic Growth on Cu Substrate As shown in Figures 10.21 and 10.22, some IMC thickness values, notably those for short and long holding times, deviate from the least square fitted average growth line. Figure 10.24 shows the deviations of experimental thickness values from the least squares fit values for the SnAgCu alloy. It is clear that the deviations are indeed the greatest on a percentage basis at short and

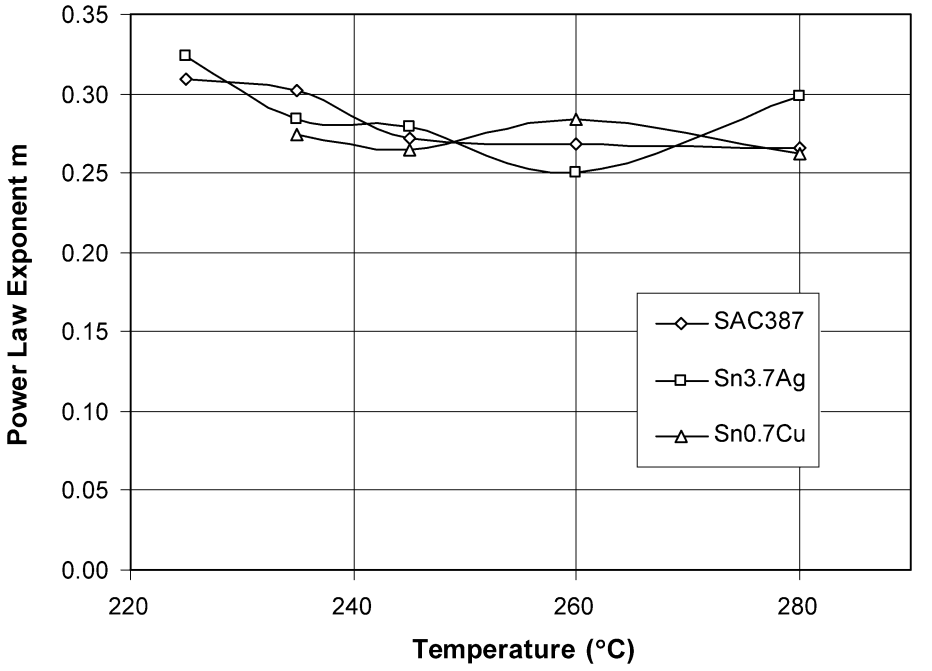

FIGURE 10.25. Calculated power (m) for IMC growth as a function of temperature for the SnAgCu, SnAg and SnCu alloys.

long times and that they are the greatest for the lower temperatures. The deviation at short times is probably the result of several factors. During the early stage of IMC formation, the IMC layer is in most cases growing into solder not saturated with copper. Also, the early stage of layer formation may be reaction controlled instead of diffusion controlled. Diffusion models [24] of steady state intermetallic growth of Cu_6Sn_5 between Cu and pure Sn and Sn containing solders also predict power law dependency rather than parabolic dependency.

The thickness (w) data shown in Figures 10.19–10.22 can also be fit by regression analysis with an equation of the form,

$$w = kt^{m(T)}, \tag{10.5}$$

where k and $m(T)$ are constants resulting from the fits. Figure 10.25 shows $m(T)$ values extracted from curve fits as a function of temperature for all three alloys studied. It can be seen that values of m vary from 0.25 to 0.32. The values are consistent with those predicted by diffusion models [25,26]. Figure 10.26 shows calculated best fit curves based on both Equations (10.3) and (10.5) for IMC growth for the SnAgCu alloy at 225°C. As can be seen, the parabolic ($m = 0.5$) curve fits the data best at time interval of 30 sec up to 2 hrs, while the power law equation works best for short times below 30 sec and again at longer times. Similar results were observed at other temperatures for the SnAg and SnCu alloys.

10.2.4.4. Intermetallic Growth on Nickel and Alloy 42 Substrates Unlike extensive study on intermetallic growth of lead-free solders on Cu substrate, there is relatively little study on other substrates. Experiments for intermetallic kinetics of SAC387 alloy were reported

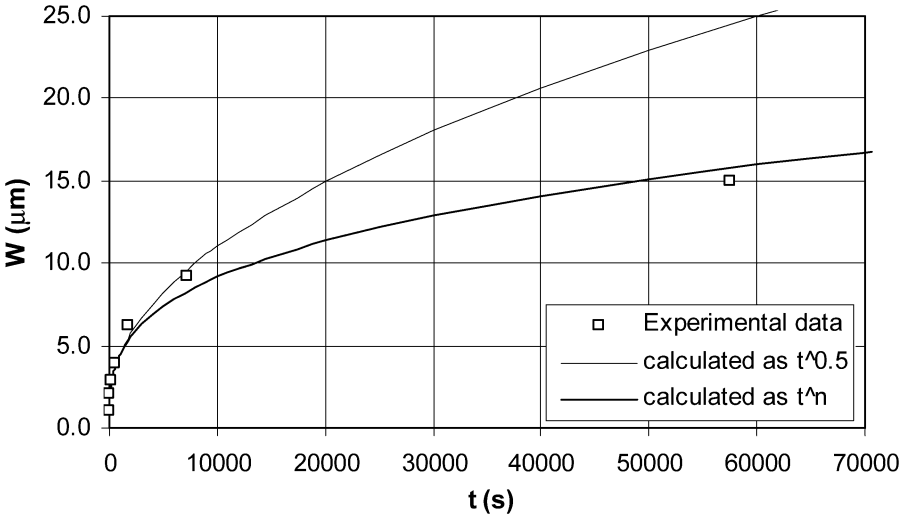

(a)

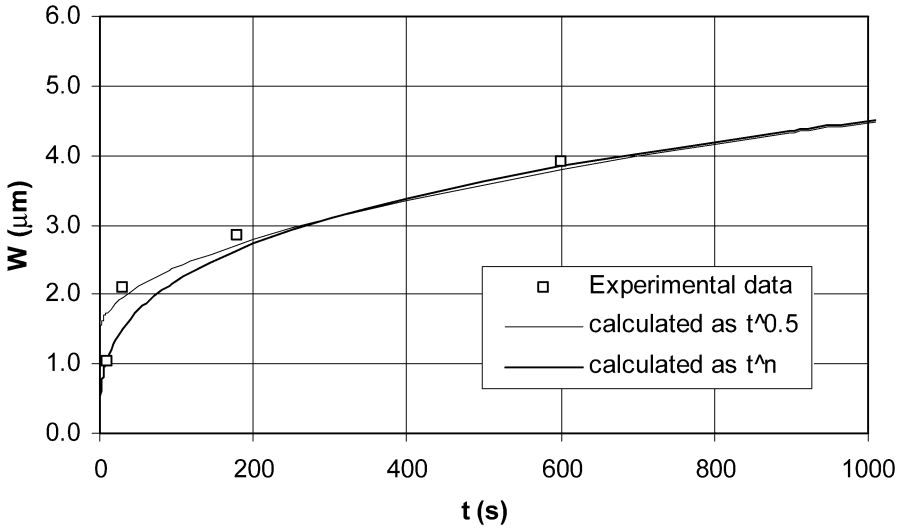

(b)

FIGURE 10.26. Comparison of two calculated lines ($w = w_o + kt^{0.5}$ and $w = kt^n$) with experimental data for IMC growth for the SnAgCu alloy at 225°C. The graph (b) presents the magnified portion of the graph (a).

for nickel and Alloy 42 (Fe-42Ni) substrates. The comparison of the intermetallic thickness as function of time at different temperatures is presented in Figure 10.27. SEM images of the intermetallic layers for the Nickel and Alloy 42 are presented in Figures 10.28 and 10.29. It can be seen that intermetallic thickness of alloy 42 samples is significantly thinner compared with those on both copper and nickel substrates.

Kinetic parameters of the intermetallic formation were calculated for Nickel substrate. The values of parameter $m(T)$ in Equation (10.3) for temperature interval of 225°C to 260°C is about 0.475. The calculated activation energy Q for IMC growth for SAC387 alloy on the Nickel substrate is equal to 12.6 kJ/mol, which is 24% lower compared with Q

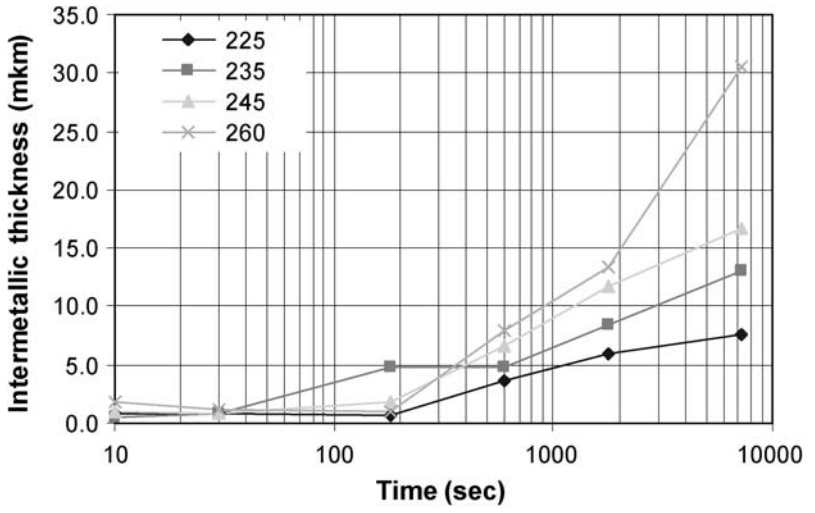

(a)

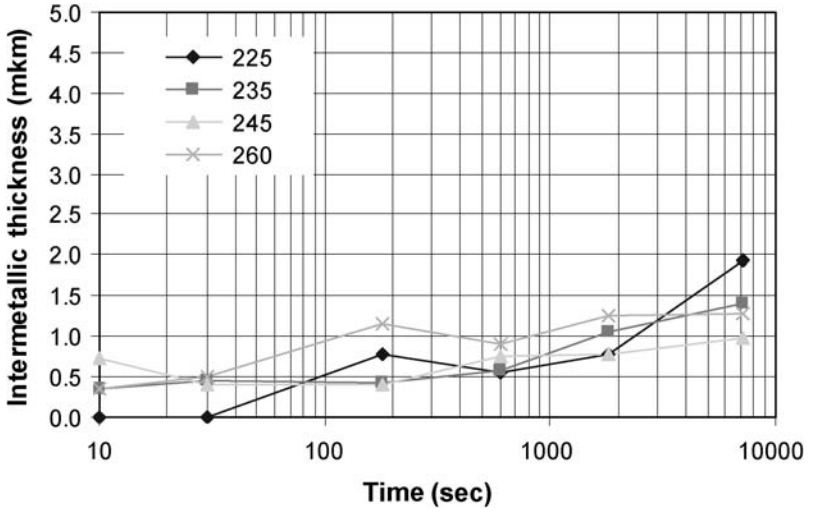

(b)

FIGURE 10.27. Thickness of intermetallic as function of time for SAC387 on (a) Nickel, (b) Alloy 42.

for copper substrates. Due to the large scattering for thin intermetallic layer measurement on the Alloy 42 substrate, statistically meaningful growth kinetic equation is not available.

Sn-Ni binary systems have three stable intermetallic compounds, Ni_3Sn (at Ni-rich side), Ni_3Sn_4 (at Sn-rich side), and Ni_3Sn_2 in the between [27]. The additions of Ag and Cu further complicate the metallurgy at the interface for Sn-Ag-Cu solder alloys. Figure 10.30 shows the EDAX phase composition for the IMC for SAC387 on the Ni substrate, indicating a compound of possible $(NiCu)_3Sn_4$ composition. No Ni-rich ICM is detectable in the samples tested.

For Alloy 42 substrate (see Figure 10.31), the alloy itself is a mixture of α-Fe plus Fe_3Ni compound. Since atomic Ni is not available, the intermetallic phase at the interface of SAC387 and Alloy 42 would be mainly Sn-Fe intermetallic compounds. The Fe-Sn

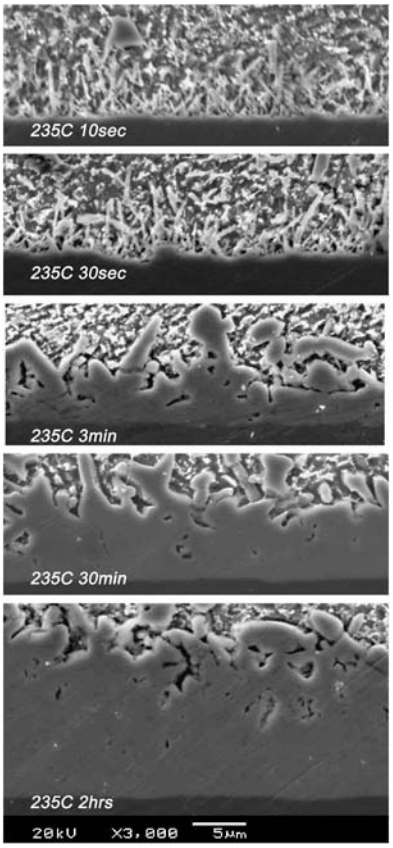

FIGURE 10.28. Comparison of SEM images of the intermetallic layers for the Ni samples cast at 235°C held for 10 sec, 3 min, 10 min, and 2 hrs.

binary system has two stable intermetallic phases: FeSn at the Fe-rich side and $FeSn_2$ at the Sn-rich side. The EDAX analysis clearly shows a $FeSn_2$ intermetallic compound is the predominant ICM for SAC387 on Alloy 42 substrate.

10.2.4.5. Summary on Intermetallic Growth Kinetics In summary, the IMC formation and growth at liquid Pb-free solders and solid interface shows the following characteristics:

(1) Morphologically the formation and growth of IMC layers between all three Pb-free alloys and copper substrate are identical, with formation of a thin layer of Cu_3Sn adjacent to the copper substrate and a scalloped layer of Cu_6Sn_5 between Cu_3Sn and the molten solders.
(2) The IMC layer formed with the SnAgCu alloy grows faster than those formed with the SnAg and SnCu alloys on Cu substrates.
(3) The faster growth of the IMC layers for the SnAgCu alloy may be the result of the layers growing into a solder initially containing more copper for the SnAgCu alloy.
(4) The thickening of the IMC layers in all alloys can largely be described with a parabolic ($m = 0.5$) growth equation on both Cu and Ni substrates, indicating a diffusion controlled growth process.

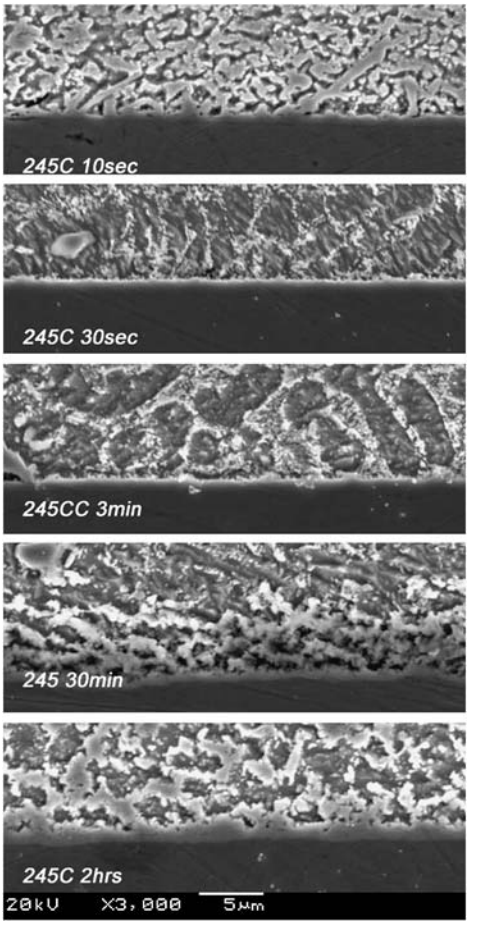

FIGURE 10.29. Comparison of SEM images of the intermetallic layers for the alloy 42 samples cast at 245°C held for 10 sec, 3 min, 10 min, and 2 hrs.

(5) Among Cu, Ni and Alloy 42, Cu substrates grow intermetallic layers fastest, followed by Ni, and Alloy 42.

10.3. LEAD-FREE SOLDERING PROCESSES AND COMPATIBILITY

As Pb-free soldering moves from the laboratory to the manufacturing floor and the worldwide electronics industry gradually implements Pb-free soldering in printed circuit board (PCB) assemblies, it becomes clear that lead-free processing has many unique requirements during to the metallurgical and chemical attributes of Pb-free solders, fluxes and pastes. Volume manufacturing with lead-free solders is a complex undertaking for the industry. As shown in Figure 10.32, there are many compatibility issues needed to be concerned in volume manufacturing of lead-free solder PCB assemblies, including processing, materials, components, equipment, design, quality control and reliability.

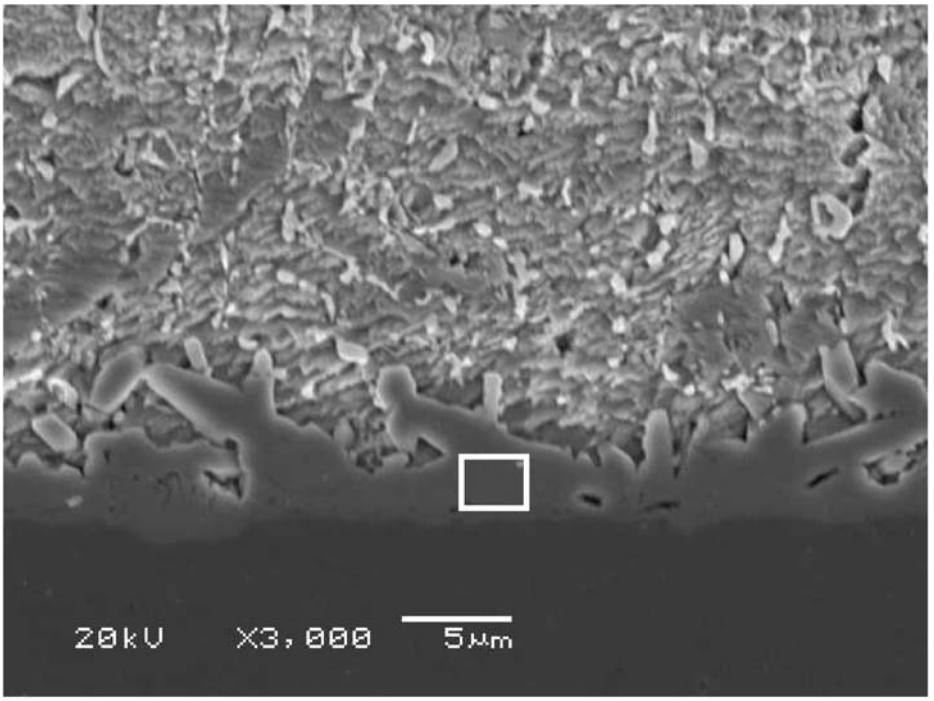

Element	Wt %	At %
AgL	0.86	0.79
SnL	64.27	48.78
NiK	8.41	12.95
CuK	26.46	37.48

FIGURE 10.30. Nickel sample (254°C, 30 min, ×3000).

10.3.1. Lead-Free Soldering Materials

10.3.1.1. Lead-Free Solder Alloy Compositions As discussed above, the industry is now converging on Sn-Ag-Cu (SAC387, SAC396 and SAC305) ternary eutectic alloys for reflow processes, and Sn-Ag-Cu or Sn-Cu eutectic alloys for wave soldering. It is generally believed that the different variations of the Sn-Ag-Cu alloys, with Ag content from 3.0% to 4.0%, are all acceptable compositions. The Sn-Cu alloy has been found to be inferior to Sn-Ag-Cu in terms of wettability, dross formation, and reliability; however, its much lower cost as compared with Sn-Ag-Cu alloys makes it an attractive alternative alloy for wave soldering, especially for cost sensitive products. The steep slope of the Sn-Cu binary phase diagram (approximately 30°C change in liquidus for every percent change in composition, roughly 20 times the slope for Sn-Pb) suggests that the chemical composition of the Sn-

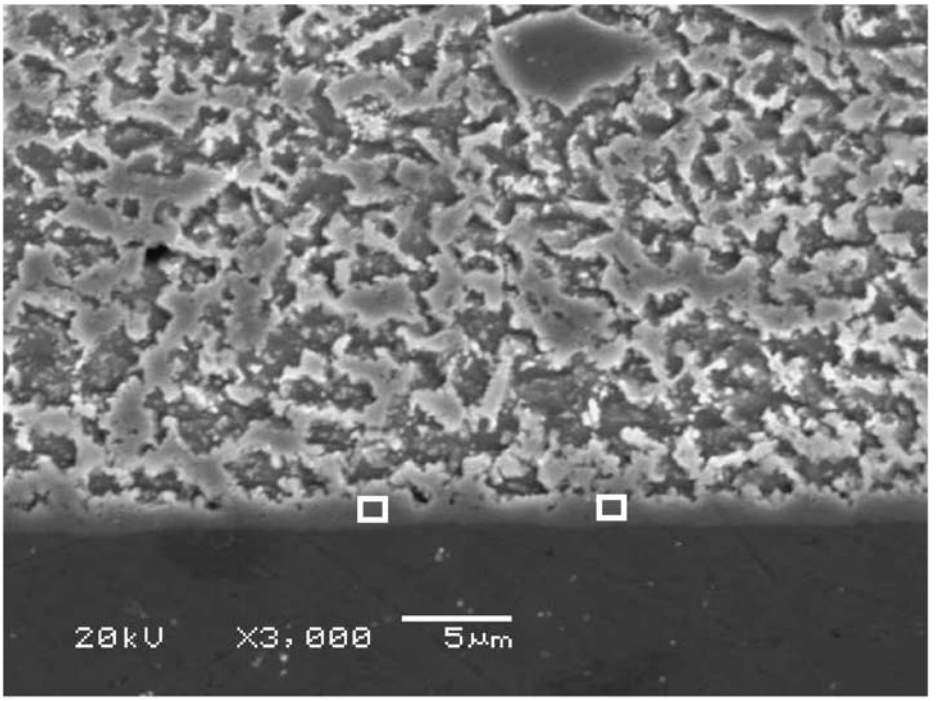

Element	Wt %	At %
AgL	0	0
SnL	80.11	65.83
FeK	16.17	28.24
NiK	1.77	2.94
CuK	1.94	2.98
Total	100	100

FIGURE 10.31. Alloy 42 sample (245°C, 2 hrs, ×3000).

Cu solder pot needs to be closely monitored and controlled. Several variants of the Sn-Cu alloys have also been introduced, including Ag, Ni, and others as alloying elements.

During the transition, many products may be assembled with lead-free solders with Pb-containing component termination. For wave soldering, the level of Pb in the solder pot, due to dissolution of Sn-Pb plated component finishes, needs to be monitored. The impact of Pb in Pb-free solders on long-term reliability is not clearly known at the current time. Preliminary studies have indicated that the impact varies with the amount of Pb in

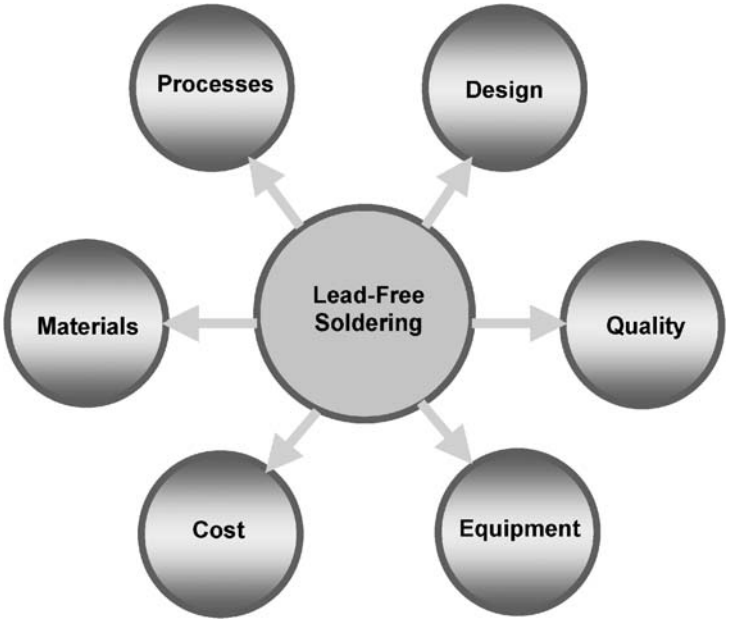

FIGURE 10.32. The compatibility issues with Pb-free soldering technology.

the solder joints, and the impact may be the greatest when the amount of Pb is within some intermediate range, because of the formation of segregated phases (e.g., coarse Pb grains) in the last-to-solidify inter-dendritic Sn grain boundaries, where cracks may initiate and propagate under cyclic loading. It has been shown [28] that 2%–5% Pb can be detrimental to the fatigue life of Pb-free solder joints.

10.3.1.2. Lead-Free Flux and Pastes Earlier attempts to simply mix the no-clean flux (developed for Sn-Pb alloys) with the Pb-free alloys yielded miserable results. The no-clean flux needs to be re-formulated for the Pb-free alloys in order to accommodate the characteristics of the Pb-free alloys. The chemical reactions between the flux and the solder alloys in the paste affect the rheology characteristics of the solder pastes (which is critical for printing performance). The difference in the density between the Pb-free solder alloys and the Sn-Pb alloys means that the metal loading of the solder paste needs to be different. The higher soldering temperature needed for the Pb-free solders also requires greater stability of the flux chemistry at higher temperatures. The performance of the flux residues after reflow, in terms of in-circuit test (ICT) probeability and electromigration, is also an important consideration. Similarly, no-clean and VOC-free fluxes need to be formulated specifically for lead-free wave soldering. Water-soluble fluxes for lead-free solder pastes and wave soldering applications are also needed for certain applications.

10.3.2. PCB Substrates and Metalization Finishes

As the soldering temperature increases, the CTE (coefficient of thermal expansion) mismatch between the laminate material, the glass fiber, and the Cu, will exert greater stresses on the Cu, potentially causing failures by cracking the Cu in the plated vias and holes. This is a rather complex issue because it depends on a number of variables, such as

the thickness of the PCB, the laminate material, the soldering profile, the Cu distribution, the via geometry (such as aspect ratio), etc. Other issues, such as delamination and blistering at higher soldering temperatures, are also areas to be studied. Much work is needed to determine under what conditions, alternative laminate materials (such as high T_g, low CTE, and high decomposition temperatures) to the traditional FR4 may be needed for Pb-free soldering. This is not to say that lower cost materials (such as CEM, FR2, FR4, etc.) can not be used with Pb-free soldering. In fact, such applications do exist in volume manufacturing with lead-free manufacturing. The situation needs to be examined on a case-by-case basis.

The search for PCB surface finishes as alternatives to HASL (hot air solder leveling) has been on-going for many years, primarily because of the inherent inconsistency in the quality of the HASL finish. For example, the thickness (and therefore solderability) of HASL is difficult to control. In areas with a very thin layer of HASL, consumption of Sn by the formation of Sn-Cu intermetallic compounds will render the areas non-wettable. The HASL finish is typically non-flat (with a dome shape), making it difficult to deposit a consistent amount of solder paste during solder paste printing and difficult to place fine pitch (<25 mil) devices. The HASL process itself is not as clean and easy to control as other plating processes. The move towards Pb-free soldering has provided the additional impetus towards Pb-free surface finish alternatives.

Pb-free HASL, using Pb-free alloys (such as Sn-Cu, Sn-Ag, or Sn-Ag-Cu alloys) in place of Sn-Pb, is commercially available. Electroless nickel and immersion gold (ENIG) provides good solderability and contact/switch interfaces for most applications; however, tight plating process control is necessary in order to prevent the occurrence of catastrophic "black pad" failures. For higher end applications, electrolytic nickel (Ni) and gold (Au) provides a more reliable surface finish. Care must be taken to limit the thickness of Au, as too much Au dissolved in the solder joints may cause "Au embrittlement," even though the Sn-Ag-Cu alloys are less sensitive to Au embrittlement than the Sn-Pb alloys. Immersion silver is a more recent and less costly alternative. Its solderability, ICT probe-ability, and contact/switch pad performance, are not as good as Ni/Au, but are adequate for most applications. For immersion Ag, the exact chemistry, thickness, surface topography, as well as the distribution of organic constituents within the Ag layer, should be carefully selected and specified [29–32].

For Pb-free soldering, immersion tin and Ni/Au surface finishes provide the best wetting results on fresh boards, followed by immersion Ag and organic solderability preservative (OSP). However, in a humid condition, the wetting of the immersion Sn finish degrades the fastest, whereas the wetting of the Ni/Au remains excellent as evidenced in Figure 10.33 to Figure 10.34, which show the relative maximum wetting force on 1 inch by 0.5 inch wetting coupons with Sn, OSP and Ni/Au finishes before and after a one-week aging at 85°C/85%RH. The Ni/Au finish remains excellent with variety of pre-conditioning treatments and heat exposures, while OSP loses wettability rapidly with exposure to a high temperature environment, as shown in Figure 10.35. Fresh immersion Ag boards can withstand up to four lead-free reflow cycles before the final reflow soldering process, and at least two reflow cycles before wave soldering process. On the other hand, neither fresh nor aged immersion Sn finished boards can withstand multiple lead-free reflow cycles or a reflow cycle prior to wave soldering process without significant degradation in wettability.

10.3.3. Lead-Free Soldering Processes

10.3.3.1. Reflow Soldering In terms of printability, tackiness, slump, and solder balling, there is no clear and consistent difference between Sn-Pb and Pb-free solder pastes, because

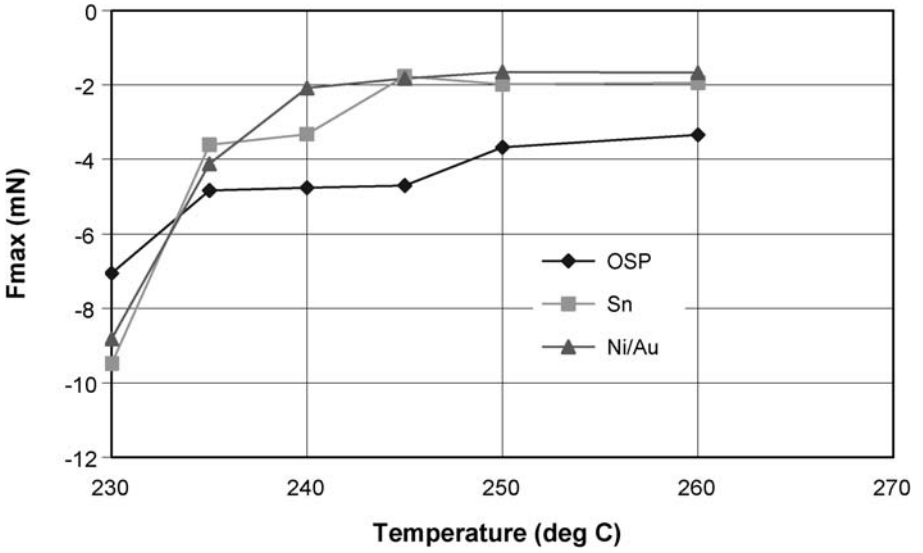

FIGURE 10.33. Relative maximum wetting balance force for virgin coupons with OSP, Sn and Ni/Au finishes (coupons size 1 inch by 0.5 inch).

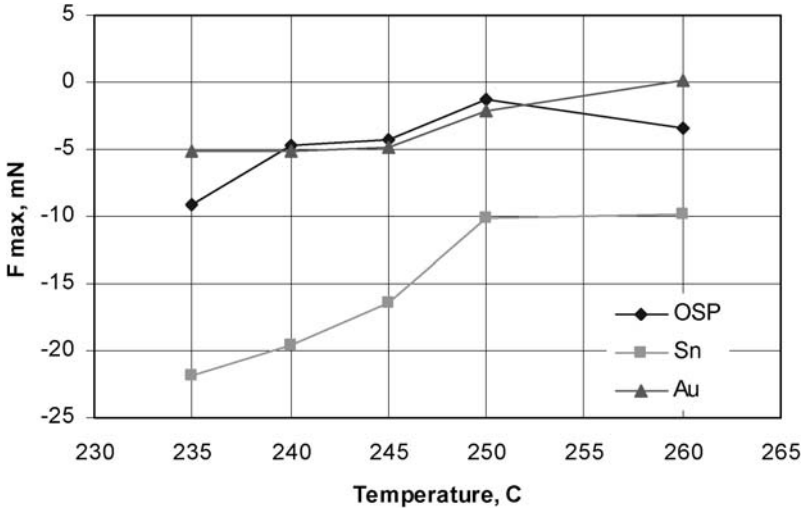

FIGURE 10.34. Relative maximum wetting balance force for coupons after aging at 85°C/85%RH.

the performances depend mainly on the solder paste formulation, not directly on the solder alloys. Very clear and consistent differences have been observed, however, in wettability between Sn-Pb and Pb-free solder pastes. In general, as expected and discussed in the previous section, the wettability of Pb-free solder pastes are not as good as Sn-Pb eutectic solder pastes on most metalization finishes [33,34]. The current commercially available Pb-free solder pastes exhibit very limited spreading on OSP during reflows up to 250°C. Exposed corners on OSP boards after reflow are quite common, unless overprint or round corner pads are used. The key parameters for the reflow profile are the peak temperature and time above the liquidus. Adequate super-heat reflow temperature above the liquidus is needed

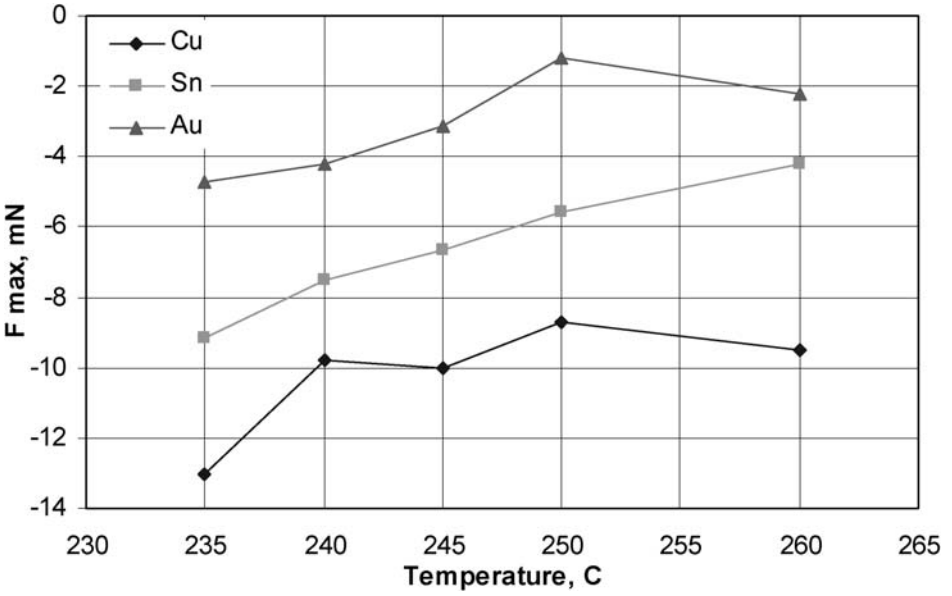

FIGURE 10.35. Relative maximum wetting balance force for coupons after aging at 130°C for 24 hrs.

for the Pb-free solder to melt, wet and spread, metallurgical reactions with the Cu or other metallic surface on the pads and the component termination to form strong intermetallic bond when cooled and solidified [35]. Typically, 30°C superheat (above the melting temperature) is desired. For Pb-free soldering, because of concerns about the thermal stability of the components, efforts have been made to minimize the soldering temperatures. For SAC alloys with the eutectic temperature at 217°C, many experimental studies show that the minimum reflow peak temperature should be 235°C for large volume manufacturing, taking into account process robustness, yield, variety of component finishes, oven thermal stability and tolerance, etc. The dwell time (or time above liquidus) is typically 40–90 seconds. The reflow profiles may be straight ramp, or with a pre-heat plateau for the purpose of homogenizing the temperature distribution across the board, with soldering environment either in air or N_2.

10.3.3.2. Wave Soldering For wave soldering with Pb-free solders, a higher solder pot temperature, typically 255–270°C, will be required. Flux application (spray or foaming), flux amount, preheat temperature, and dwell time needs to be optimized for each particular Pb-flow wave soldering application. A longer pre-heat may be needed in order to keep the thermal shock (difference between the preheat and peak temperatures) below 100°C to protect ceramic components. Dual wave soldering, already popular in Sn-Pb soldering, will still be used for Pb-free solders, and inert (N_2) atmosphere may be used to improve yield and reduce dross.

The amounts of dross formed with SAC and Sn-Pb solders have been found to be very similar, at the same temperature, for the same duration, and under the same atmosphere, while the Sn-Cu solder forms considerably more dross. Just as with the Sn-Pb solder, N_2 helps reduce dross formation for Pb-free solders. The overall influences on the yield and quality for wave soldering of other process parameters, such as conveyor speed, dwell time and contact length, component orientation and soldering direction (parallel or perpendic-

ular), are similar for Pb-free and Sn-Pb solders [36,37]. For Pb-free wave soldering, the chemical composition of the molten solder in the pot needs to be closely monitored. For the Sn-Cu solder, the liquidus temperature will change by as much as 6°C when the Cu composition changes by 0.2%; such a change may cause significant change in the wave dynamics and the soldering quality.

10.3.3.3. Rework and Repair Rework for Pb-free solders has been found to be generally more difficult, because the Pb-free solder alloys typically do not wet or wick as easily as the Sn-Pb solder. In spite of the difficulty, successful rework methods (both manual and semi-automatic) have been developed with Pb-free solders for all types of components (discrete components, area array packages, etc.). The soldering parameters should be adjusted to accommodate the higher melting temperature and less wettability of the Pb-free solder. Care should also be taken to minimize any potential negative impact of the rework process on the reliability of the components and the PCBs. Surface insulation resistance (SIR) tests need to be performed to ensure the compatibility between the reflow/wave solder flux and the rework flux.

The issue of "component mixing" or cross-contamination warrants special attention, especially during the transition period. If a Pb-bearing board is to be repaired (for example for warranty repair at some future time) with the Pb-free solder, the repair temperature impact on the Pb-bearing components (especially plastics package parts) and PCBs would be a concern, with further reliability implication of non-homogeneous mixing of Pb-free solders and the original Sn-Pb solder. Careful consideration should be given to the use of area array packages with Pb-free balls to repair a Pb-board. In this case, if the temperature is not high enough, reliability concerns may also arise.

10.3.4. Components for Lead-Free Soldering

10.3.4.1. Termination Metallurgy Traditionally, most of the components have Pb-bearing lead finishes or terminations (for chip capacitors/resistors), or Pb-bearing solder balls, to provide and to preserve solderability. A number of Pb-free component termination finishes have been evaluated and used over the years, including Ni/Pd, Ni/Au, and Ni/Pd/Au for lead frames (such as QFP). More recently, Sn-Bi, Sn-Cu, and Sn-Ag-Cu-Bi coatings were proposed and evaluated for Pb-free component lead finishes and terminations with some successes. Due to its processing compatibility to current Pb-bearing finishes/terminations and good solderability, matte Sn as component termination finishes have been the preferred termination metallurgy for many component designers and manufacturers. Although it has been used for passive components (such as chip capacitors and resistors) for many years, pure tin for Pb-free fine pitch component lead finishes have waved a red flag for many OEMs with higher reliability requirements due to ramifications related to the possible Sn whiskering.

10.3.4.2. Tin Whiskering The issue of Sn whisker formation and growth on pure Sn finish has generated a great deal of concern, especially for fine pitch QFPs and for high reliable and long service life products such as those used in avionics, aeronautics, satellites, missiles, mission-critical storage systems and servers, as well as medical systems. Tin whiskering currently is one of most difficult issues for the implementation of a complete Pb-free transition. Although, it is generally agreed that the root cause of Sn whisker growth is the compressive stress which builds up in the Sn coating after plating, the origins and magnitude of such stresses and kinetics of Tin whiskering are still not fully understood. It has

been reported in the literature that whiskering phenomenon is dependent on grain size, organic (carbon, sulfur, oxygen) and inorganic inclusions in the tin coatings, plating conditions (current density, pulse, temperature, time), residual stress, external stress, thermal stresses, substrate materials, surface oxides and roughness, environments, even electric and magnetic field. Field failures attributable to tin whiskers have resulted in many million, if not billions, of dollar loss in mission critical communication satellites. The tin whiskers have been described in the press [38] to be a potential problems similar to Y2K issue, should Sn-coated components go into every electronic and semiconductor products due to the requirements for elimination of lead in any form in electronic products.

In terms of tin whiskering mechanisms, it has been reported that whiskers be controlled by the Sn/Cu interfacial reactions, such as intermetallic growth, inter-diffusion, which lead to buildup of compressive stress in the tin coatings either through volume change of intermetallic formation and growth [39], or excessive Cu diffusion into the Tin at the interface. If the oxide films on the tin coating surface is porous and broken, whiskers will initiate and grow to release the compressive stresses. However, these theories fail to explain why a small amount of alloying elements, such as Pb and Bi, is able to eliminate or significantly reduce the tin-whiskering since there is no noticeable change in the Sn/Cu interfacial reactions.

In order to understand the fundamental physical and mechanical metallurgy for Tin whisker initiation and growth, it has been proposed recently to use nano-indentation to induce tin whiskers on pure tin coated component leads [40]. The indentations generate variable small scale compressive stress–strain field with sharp stress gradient. The nucleation and growth of whiskers were monitored *in-situ* with ESEM. Finite element analysis was carried out to theoretically calculate the stress/strain distribution around the indentations and to identify the stress level at which whiskers nucleate. Experimental and theoretical calculation results show that whiskers form at a certain stress level and locations. This suggests that there might exist a critical stress that governs the whisker initiation. It is believed that establishment of a quantitative relationship between stress level and whisker formation/growth could lead to a breakthrough in risk and reliability assessment with pure Tin application in the electronic industry and in safeguard for smooth Pb-free transition. In additions, a joint research project [41] was established recently to use vapor deposition techniques to make thin Cu and Sn coatings with a variety of thickness on silicon wafers, then use a curvature based optical method (Multi-beam Optical Stress Sensor—MOSS) to measure stress evolution in the Sn film following deposition and during aging. Any stress build up due to any reason in the thin film system will cause the whole thin silicon wafer to bending (change in curvatures). Coupled with study of the microstructure evolution, interfacial reactions, and monitoring whisker initiation and growth kinetics, we might be one step closer to fully understanding the intrigue tin whiskering phenomenon.

The current strategy to reduce or mitigate the risk of Sn whisker is generally based on empirical observations, including:

(1) Matte Sn instead of bright Sn;
(2) Sn alloys with a small percentage of alloying elements, such as Bi, Ag and Cu;
(3) Ni barrier layer underneath Sn coating;
(4) Reflowing Sn coating or annealing;
(5) Conform coating or strip of Tin coatings.

The effectiveness of these and other mitigation techniques are still under evaluation by the industry. Accelerated testing methods and acceptance criteria for pure tin coated components have been proposed by JEDEC and IPC recently [42]. However, since it is not

able to definitely assess the accelerating factors for most proposed acceleration and acceptance tests, the real risk associated with Tin whiskers in the vast different field application conditions will still be unknown. It is hoped that as the tin whiskering mechanisms are understood better in the future, with better measuring and monitoring methodologies and systems being developed, the real solutions may be eventually developed to eliminate or reduce the tin whiskering problems.

10.3.4.3. Component Thermal Stability Different components have different sensitivities to the soldering temperature. For example, ceramic resistors and especially capacitors are very sensitive to the ramp rate but are not so sensitive to the actual temperature. Aluminum electrolytic capacitors, on the other hand, are extremely sensitive to temperatures. Connectors and some of the plastic package parts may also exhibit increased failures (such as delamination, pop-corning, deformation, etc.) at higher soldering temperatures. Roughly, for every 10°C increase in temperature, the MSL (moisture sensitivity level) degrades by one level.

Because of the temperature impact on components, conscious efforts have been made to minimize the Pb-free soldering temperatures. However, as discussed above, the soldering temperature have to be high enough to offer a robust process window to enable good yields for large volume production for a variety of products. For reflow soldering, assuming the minimum peak reflow temperature to be 235°C for a specific product with a specific solder paste, the actual maximum temperature will be still dependent on the board size, thickness, layer count, layout, Cu distribution, component size and thermal mass, thermal capacity of the oven and certain unavoidable process variations. Large thick boards with large complex components (such as CBGA, CCGA, etc.) typically have temperature delta as high as 20–25°C [43,44]. Rework is another process which needs to be conducted at an even higher and non-uniform elevated temperature environment. For wave soldering, the solder pot temperature is typically higher than the reflow temperature.

When all of the application requirements are taken into consideration, 260°C peak temperature has been proposed as the temperature required for components for Pb-free soldering. It is recognized, however, that for certain products (such as small/medium boards), which typically have a smaller temperature delta, a lower maximum temperature may be adequate. The actual component body temperature may be different from the temperature measured on the board, and different components may have different temperatures depending on component thermal characteristics and location on the board. Overall, most components may have to be qualified for temperatures as high as 260°C.

10.3.4.4. Component Forward/Backward Compatibility Sn, Ni/Pd and Ni/Pd/Au finished components are forward compatible with Pb-free soldering, as well as backward compatible with the Sn-Pb solder in terms of soldering processes. This makes it much easier to manage production lines with Sn-Pb solders and Pb-free solders within the same factory during the transition. The backward compatibility of SAC solder balls with Sn-Pb soldering, however, is very much questionable. This is primarily due to the fact that the SAC alloys may not always completely melt during reflow with the Sn-Pb solder, typically at reflow peak temperatures between 205–225°C (or even as low as 200°C in extreme cases). As such, there will be little or no self-alignment, which is critical especially for finer pitch area array packages, with coplanarity issues further aggravating the situation due to the lack of collapse. Further, very little mixing takes place leading to grossly segregated and non-homogeneous solder microstructures. Poor interfacial bonding and increased voids are some of the issues, which may render the SAC balled area array packages "incompatible" with the current Sn-Pb soldering [45,46]. When the reflow temperature is high enough

(>230°C) and self-alignment does occur, alloy mixing and composition homogenization takes place between the SAC and Sn-Pb, and the reliability of the interconnects using Sn-Pb solder paste and SAC balls can be as good as that using Sn-Pb solder paste and Sn-Pb balls for area array packages.

10.3.5. Design, Equipment and Cost Considerations

It is anticipated that no major changes in design rules will be needed when switching to Pb-free soldering. For wave soldering of through-hole components, some changes in the design may be necessary to accommodate the difference in the physical properties between Pb-free and Sn-Pb solder alloys. The general guidelines, such as board orientation relative to the soldering direction, still apply to Pb-free wave soldering [36,37].

As with the Sn-Pb solder, it is beneficial to optimize board layout and Cu distribution in the PCBs in order to minimize the temperature delta across the board. This is especially important for Pb-free soldering in order to minimize the temperature impact on components.

For reflow ovens, the ability to minimize the temperature delta for large complex boards is a key differentiator for Pb-free soldering. It has been suggested that in order to minimize the temperature delta, the convey speed should be lowered for the Pb-free reflow process. This, however, is limited, not only by the throughput requirement, but also by the durability of the flux and by the dwell time.

Wave soldering machines need adequate pre-heating capacity in order to keep the thermal shock below 100°C. Solder pot erosion is another consideration for Pb-free wave soldering, and special materials are needed for the solder pot and the other equipment components which are in contact with the molten Pb-free solder. Most of the rework equipment for Sn-Pb can still be used for the Pb-free soldering.

Even though the types of defects for Pb-free solders, for both reflow and wave soldering, are the same as for Sn-Pb, it takes considerable efforts in order to achieve the same yield, especially for wave soldering. This is especially true during the transition when every party of the supply chain has to go through the learning curve. AOI, AXI, and ICT parameters will need to be adjusted for Pb-free solder boards to pick up defects due to poor printing and poor wetting in Pb-free soldering processes.

It is generally accepted that the IPC 610 standards are still valid for Pb-free solder PCBA for workmanship acceptance. Discussions are currently on-going to further refine the standards for Pb-free soldering. Operator (and AOI) training is needed for Pb-free soldering because the appearance of the Pb-free solder joints are generally more dull and grainy, and less shiny, than the Sn-Pb solder joints. As discussed previously, this difference in appearance is determined by the metallurgy of the solder alloys and is not a reflection of the workmanship. The Sn-Pb solder solidifies as a typical eutectic microstructure. The SAC alloy, even though it is a eutectic alloy, solidifies as an off-eutectic microstructure, under typical soldering conditions, due to non-equilibrium solidification. Sn dendrites with shrinkage, which are formed as a result of the non-equilibrium solidification, create the grainy and dull appearance of Pb-free solders joints.

There are no simple ways to assess the precise cost impact for converting to Pb-free solders. The field is still dynamic and fluid, and volume dependency is an important factor. However, it is certain that Pb-free solder pastes cost more than the Sn-Pb solder paste. The price differential is expected to decrease as the volume increases. SAC bar solder and wire-core solder will cost several times more than the Sn-Pb solder because of the higher

metal cost for Sn and Ag. Components and PCBs for higher soldering temperatures may also add to the cost. Any special handling or baking for components will also increase the cost. In terms of oven energy consumption for reflow, study has shown that once the oven has reached steady state, the difference in power consumption between Sn-Pb and Pb-free soldering is about 10%–20% for boards of typical sizes and complexities [43]. Yield is another factor which can significantly impact cost. Equipment upgrading, if needed, is also a contributor to initial cost increase. Other cost factors are due to the complexity in managing the transition, including training, materials handling and tracking.

10.4. RELIABILITY OF PB-FREE SOLDER INTERCONNECTS

There are many published reliability results for Sn-Pb solder joints based on the field data, power/temperature cycling tests, mechanical shearing, bending, and twisting tests, shock and vibration, and electrochemical tests [47–50]. However, it is not the case for Pb-free solder joints because of limited volume production and limited variety of products manufactured with Pb-free solders.

Many environmental stress factors, such as temperature, voltage, humidity, corrosion, current density (electromigration), and mechanical loads, can lead to Pb-free solder joint failure. The most common failure modes in practice are overload and thermal fatigue. Overload failure occurs whenever the stress in the solder joints is greater than the short time mechanical strength of the solder alloys, such as in impact tests or with improper handling. On the other hand, thermal fatigue failure takes place via the initiation and propagation of cracks. The stress that typically causes fatigue failure is usually below the overload failure levels. Reliability of the Pb-free solder joints of the high-density package assemblies is dependent on temperature cycling test conditions, PCB and package materials, as well as the metalization surfaces of the components and of PCBs, such as HASL, Ni/Au, and OSP finishes.

10.4.1. Reliability and Failure Distribution of Pb-Free Solder Joints

Reliability of the solder joint of a particular package is defined as the probability that the solder joint will perform its intended function for a specified period of time, under a given operating condition, without failure. Numerically, reliability is the percentage of survivors, i.e., [51]:

$$R(t) = 1 - F(t), \tag{10.6}$$

where $R(t)$ is the reliability (survival) function and $F(t)$ is the cumulative distribution function (CDF) for failure.

Life distribution is a theoretical population model used to describe the lifetime of a solder joint and is defined as the CDF for the population. Thus, the objective of a reliability test is to obtain failure data and to best fit the failure data to the CDF of a chosen probability distribution, in the most cases, the Weibull distribution. The number of items (sample size) to be tested should be such that the final data are statistically significant.

Most reliability tests are acceleration tests in nature (with increased stress intensity, and realistic sample sizes and test times). Thus, acceleration models (to determine the acceleration factors) are needed to transfer the failure probability, reliability function, failure

rate, and mean time to failure from a test condition to a normal operating condition. In establishing the acceleration models of the solder joints, their surrounding materials (e.g., solder, molding plastic, ceramic, copper, fiber reinforced glass epoxy, and silicon), loading conditions (e.g., stress, strain, temperature, voltage, humidity, current density, and voltage), and failure mechanisms and modes (e.g., overload, fatigue, corrosion, and electromigration) must be considered. The acceleration factors are determined by the predominant material failure physics within the environmental stress range under the test and/or the operation conditions. It is possible that the predominant failure mechanism under the acceleration test condition may not be the one that is operational under the real application conditions. In these cases, the reliability models established in the acceleration tests may not be applicable in practice.

Some common tests for solder joint reliability are temperature cycling, power cycling, functional cycling, shock and vibration, mechanical shear, pull, push, bend and twist, humility, corrosion, voltage, current density, etc. In the microelectronics industry, the solder joint failure caused by temperature cycling under normal application conditions and during testing is the predominant one. Reliability tests based on actual electronic assemblies yield valuable data on the failure distribution only for the specific test condition. The reliability results also depend on the component and PCB substrate materials, and the size of the components. The results are functions of the reliability test environments. The factors that affect reliability of Pb-free solder joint interconnections in electronic assemblies are discussed in the next section.

10.4.2. Effects of Loading and Thermal Conditions on Reliability of Solder Interconnection

Thermal cycling in normal operations or stress-screening tests of electronic products generates very complicated creep/fatigue deformation and damage processes in solder joints. The current Pb-free solder candidates, such as Sn3.0Ag0.5Cu (SAC305), Sn3.9Ag0.6Cu (SAC396), and Sn3.8Ag0.7Cu (SAC387), are based on near eutectic composition of the Sn-Ag-Cu ternary system; they all have higher melting points, different mechanical properties and physical properties (surface tension and viscosity) from the current Sn-Pb eutectic based solders [52]. These Pb-free alloys tend to have a higher yield strength and a higher resistance to creep deformation [53]. From the point of view of traditional engineering design, these attributes are very much desirable since normal engineering components and structures operate well within the material elastic limits, and not much time-dependent deformation (creep or stress relaxation) is anticipated in service. However, solders and solder joints also function as a strain relief buffer for thermal mismatch between PCB substrates and components, in addition to mechanically supporting components and conducting electricity (and heat). A stronger or less ductile solder may not fit all application conditions, particularly when a large thermal strain is expected. For Pb-free and other solders, the homologous temperatures (T/T_{m}) are more than 0.6, leading to the ultimate solder joint lives to be dependent on a variety of parameters, such as initial microstructures, microstructural change during service, temperatures, frequency, holding time, solder joint geometry, as well as restraining effects from adjacent materials and structures [54].

In order to understand the actual reliability of Pb-free solder joints, time and path-dependent creep models are needed to determine the severity of the thermal mechanical loads in solder joints under different service conditions [55]. Methods to reduce such thermal loading in terms of both material properties and solder joint design for any specific ap-

plication thus need to incorporate solder alloy creep and fatigue life models, package/PCB design parameters, and anticipated service conditions.

It is important to distinguish the intrinsic and extrinsic factors that influence the reliability of a solder joint in service and in testing. For a given solder alloy, the reliability of solder joints made with a normal soldering manufacturing process is largely dependent on loading and thermal conditions that are determined by the joint geometric shape and adjacent materials' mechanical, thermal and geometric properties, as well as service or testing conditions. These factors can be considered to be extrinsic in nature. On the other hand, creep, monotonic and cyclic deformation, and resistance to fatigue and creep crack initiation and propagation, are intrinsic to a solder alloy, which are determined basically by the composition-processing-property relationship of the solder alloy.

Since solder joints in general have a complicated geometric shape and geometric discontinuity, and are generally under multi-axial stress–strain conditions, measurement of its mechanical behavior under these conditions are not possible in most cases. Fundamental material mechanical tests of solder alloys are usually conducted on laboratory samples under much simpler stress–strain conditions (uniaxial tension or torsion). These results may or may not be used directly for actual solder joint stress/strain and failure analyses due to a lack of representativeness of the actual microstructure and the actual multi-axial stress condition. Likewise, most industry reliability tests on actual solder joints with certain package design and configuration under specific test conditions may not be extended to other conditions since the solder joints are under uncontrollable and non-measurable non-uniform stress–strain condition, where both extrinsic and intrinsic factors are playing important roles in determining the final reliability lifetime of the solder joints.

Although much has been known to the commonly used Sn-Pb eutectic alloy, the reliability and life assessment methods are still far from perfection due to complicated microstructural evolution and intermetallic reactions, as well as time and path dependent creep and fatigue damage processes. For Pb-free solders, mechanical data from well controlled tests are still scarce. Comparisons between the solder joint reliability performance of different solder alloys were mostly conducted on individual components in specific geometric and thermal conditions [56–58]. Due to many other factors, such as different solder joint geometry, different thermal and mechanical properties of components and board materials, such a comparison may not be generalized, and may sometimes be misleading.

10.4.2.1. Strength of Pb-Free Alloys under Monotonic Shearing and Creep Conditions Many factors can affect the service reliability of a solder joint [59]. Among them, the deformation and fracture behavior of solder alloys under a variety of complex load conditions is foundation to understand and model the reliability performance of real solder joint interconnections. Most of mechanical study on solder alloys was conducted with real solder joints or simplified shearing tests such as sandwiched shearing samples. Due to variations in solder joint shape and small sample size, direct measurement and control of stress–strain are often not possible. Recently, mechanical shearing and creep strength of Pb-free alloy (SAC387) has been reported [60,61] based on thin-walled samples which provide a nearly uniform stress–strain condition for measurement and control, with a computer-controlled bi-axial tension-torsional servo-hydraulic system.

10.4.2.1.1. Shearing Strength of Pb-Free SAC387. Figure 10.36 shows stress–strain curves for SAC387 alloy with shearing strain rates of 6.7×10^{-7} to 1.3×10^{-1} (1/sec). It is clear that strain rates have very significant effects on general deformation behavior of SAC387. With strain rate change from 6.7×10^{-7} to 1.3×10^{-1} range, the change in both yielding stress and flow stress are running as high as high as 400%. What is clear here is

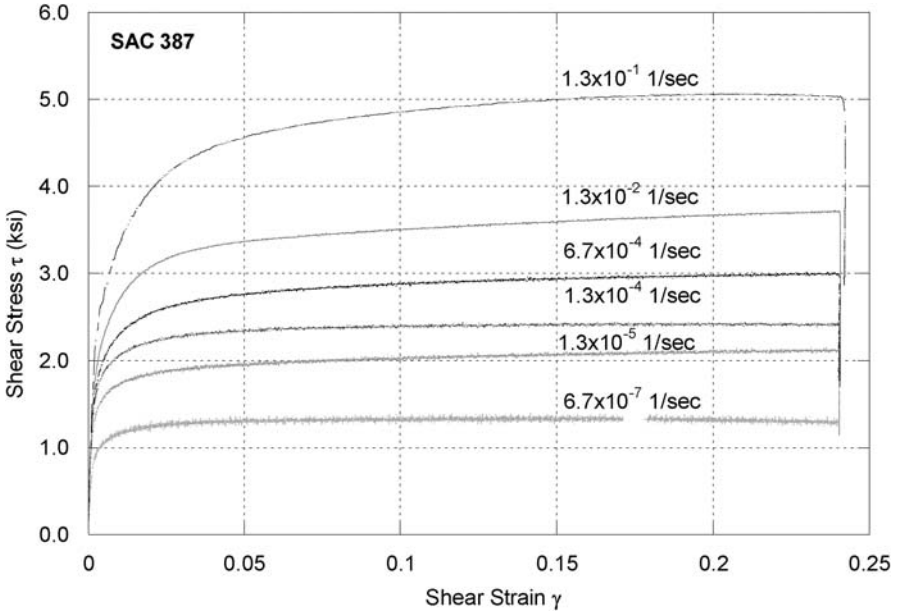

FIGURE 10.36. Strain rate effects on Pb-free SAC387 solder.

that all mechanical properties of elasticity, yielding, flow stress, or ultimate strength of Pb-free SAC387 alloy are highly strain-rate-sensitive. It is ill conceived to compare strengths of Pb-free alloys with others without indicating an exact test condition. The difference between yielding strengths and ultimate strengths, as usual, indicates how strong a material goes through strain hardening. It is clear that a much strong strain hardening occurs at higher strain rates for Pb-free SAC387 alloy.

10.4.2.1.2. Variable Strain Rate Shear Test. Variable strain rate and load drop tests on one single test sample have been a very useful mechanical test technique to develop general state variable material constitutive equations [62]. This kind of tests usually requires advanced programming capability and accurate measurement for the mechanical testing system to catch the instantaneous response of materials to sudden change in stress or strain. Figure 10.37 shows such variable strain rate test results for Pb-free SAC387 and Sn-Pb eutectic alloys. In the case of increasing strain rates [Figure 10.37(a)] from 1.3×10^{-4} to 6.7×10^{-4} to 1.3×10^{-2}, it can be seen that there is a rapid increase in inelastic flow stress after each strain rate increase, followed by gradual positive strain hardening with further increase in shear strain. The magnitude of increase in the stress at the beginning of the strain rate change (e.g., from 6.7×10^{-4} to 1.3×10^{-2}) for SAC387 is much more significant than the Sn-Pb eutectic alloy. It is clear that strengthening effects or flow stress increase is not coming only from inelastic deformation; the strain rates play a major role also.

The shear stress–strain curves for the decreasing strain rate tests (from 1.3×10^{-2} to 6.7×10^{-4} to 8.9×10^{-5} to 1.3×10^{-5}) are shown in Figure 10.37(b). Again, it can be seen that the sudden strain rate decreases cause a sharp stress drop, particularly for SAC387 alloy from strain rate of 1.3×10^{-2} to 6.7×10^{-4}. The drop in stress for both alloys takes place rapidly after a sudden decrease in strain rates.

It needs to point out that even the strain rate is reduced, there is no reverse in shear strain direction, and the inelastic strain is still increasing. It is interesting to note that after

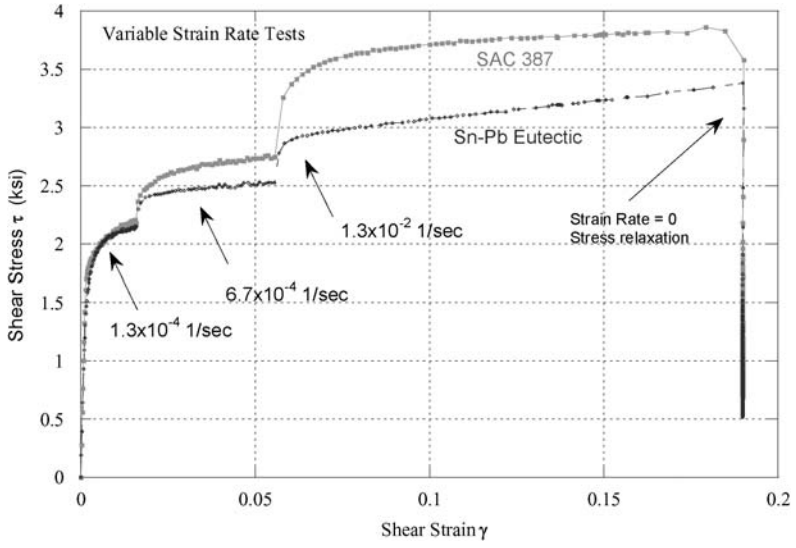

(a)

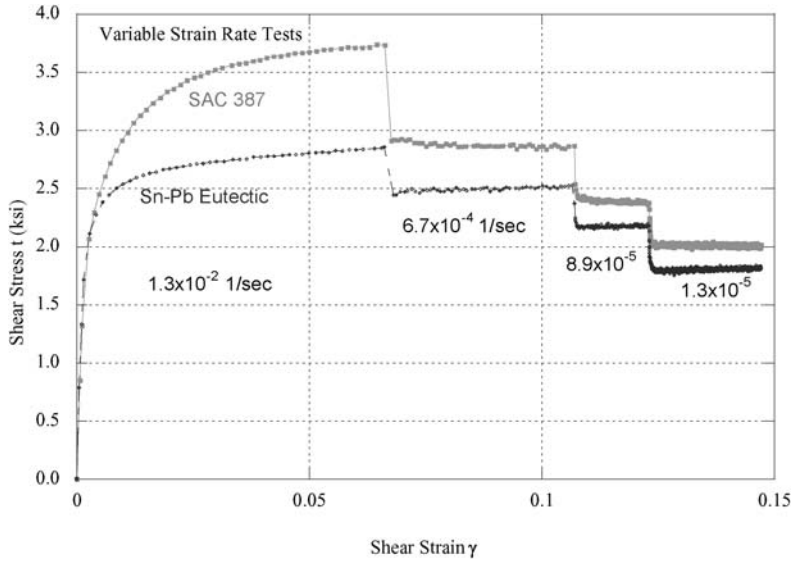

(b)

FIGURE 10.37. Variable strain rate shearing tests. (a) Increasing rates from 1.3×10^{-4} to 1.3×10^{-2}/sec. (b) Decreasing rates from 1.3×10^{-2} to 1.3×10^{-5}/sec.

the initial stress drop, SAC387 flow stress keeps dropping gradually for more than 5% more inelastic deformation at 6.7×10^{-4} after drop from 1.3×10^{-2}, while Sn-Pb eutectic shows a slight strain hardening after the initial stress drop. The next two steps of strain rate drop induce further flow stress decrease for both alloys. It is worth to know that the flow stress levels for both alloys at each strain rate are not exactly same for the two different variable tests, but generally they are within the same order of magnitude. What is interesting is that there is no normal strain hardening after the initial strain rate drop at 1.3×10^{-2} for both

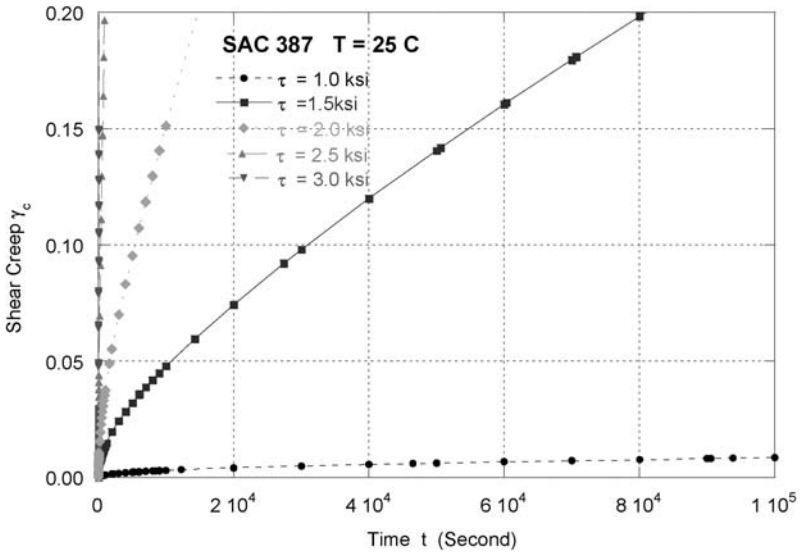

FIGURE 10.38. Shear creep curves of SAC387 solder at RT.

alloys even an additional more than 10% inelastic deformation is accumulated at the low strain rates.

It is clear that the complex stress–strain behavior for both Sn-Pb eutectic and Pb-free SAC387 alloys indicates that the classic elasto-plasticity and strain hardening theories (either isotropic or kinetic hardening) fail to model the mechanical deformation processes in solder alloys. Even if the elastic strain, inelastic strain, and strain rate are known, there is no analytic mathematic equitation to define a unique stress–strain condition. Apparently, the stress–strain is highly path-dependent. Such a behavior will need more sophisticated internal state variable approach to model, where back stress and recovery kinetic can be formulated and integrated with a given deformation history.

10.4.2.1.3. Creep. Creep deformation develops with time under a constant stress. After the initial loading, which may be purely within linear elasticity or elasto-plasticity, all further deformation is accumulative and is time-dependent. At high temperature (usually $T/T_m > 0.5$), metals undergo creep deformation. The primary and secondary stages of a creep curve are determined by a combined action of strain hardening and thermally activated recovery of dislocation obstacles [63,64]. In the primary stage, the strain hardening by formation of dislocation tangles or a dislocation substructure predominates, while the secondary stage is characterized by a balance between strain hardening and recovery softening. The acceleration of creep in the tertiary stage is often caused by formation and joining of micro-voids or cavities on grain boundaries, that is, onset of internal or external damage processes which result in a decrease in the resistance to load or a significant decrease in the effective section area to carry load [65]. The accumulative strain at each stage of creep is very much dependent on stress level, temperature, and stress condition (tensile, torsional or multi-axial stress conditions).

Figure 10.38 and Figure 10.39 show the creep curves for Pb-free SAC387 alloy and Sn-Pb eutectic alloy at different stress levels at room temperature under torsional test condition. In additions to the obvious effects of stress level on creep and creep rates, there is subtle difference in general creep behavior between Sn-Pb eutectic alloy and Pb-free

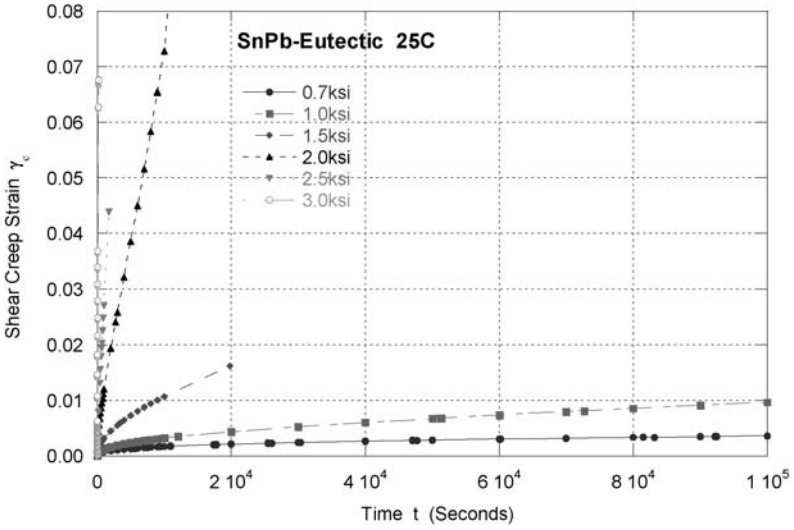

FIGURE 10.39. Shear creep curves of Sn-Pb solder at room temperature.

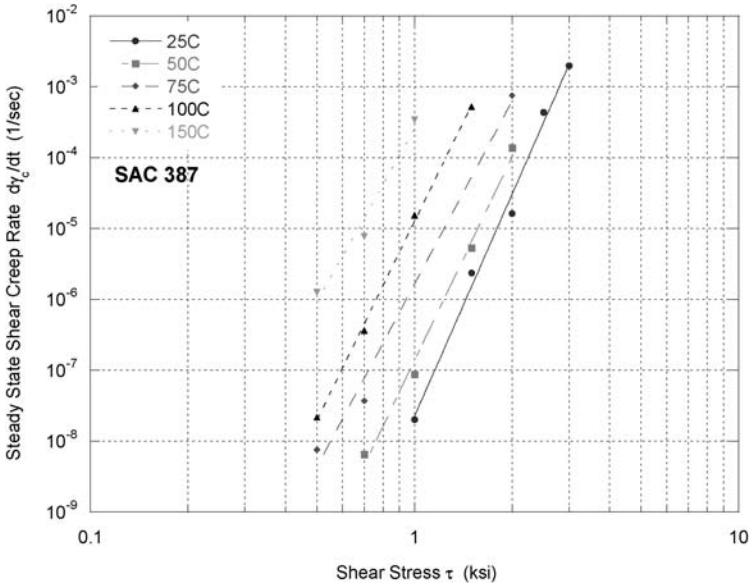

FIGURE 10.40. Shear creep rates vs stress for SAC387.

SAC387 alloy. For Sn-Pb eutectic alloy, the accumulative primary creep is relatively small (less than 1.0% for all the stress levels tested: 0.7 ksi to 3.0 ksi), and also relatively short. For Pb-free SAC387 alloy, the primary creep is a strong function of stress level. At low stress level (1.0 ksi and below), the accumulative primary creep is very low (less than 1.0%). But at high stress level, the primary creep strain can easily reach more than 5.0%, see Figure 10.38. Such primary creep behavior was also observed with other high tem-

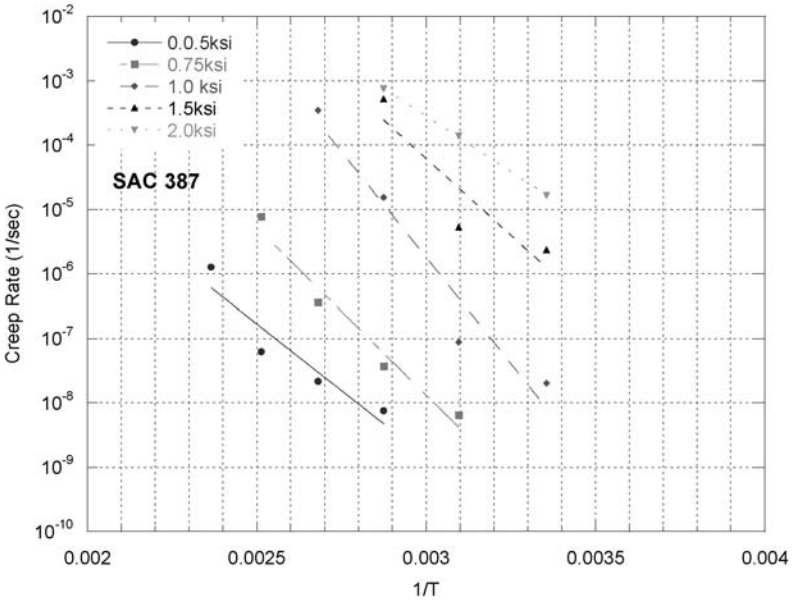

FIGURE 10.41. Temperature effects on creep rates for SAC387.

perature Pb-free and Pb-bearing solder alloys by the authors [66], which could further complicate the general mathematic modeling of creep deformation and fatigue life.

The stress dependency of the secondary (steady state or minimum) creep rates usually indicate the underlining creep mechanisms. For the SAC alloy tested, the secondary creep rates vs shear stress at temperatures ranging from 25°C to 150°C are presented in Figure 10.40. It is clear that SAC alloy shows a high stress dependency of creep rates, and follow the power creep well with the stress exponents approach 10, indicating that there could be a precipitation strengthening mechanism existing.

The temperature effects on stead-state creep rates under different stress levels for SAC387 alloy are presented in Figure 10.41. For Pb-free SAC387 alloy, the activation energy data are is scattering, but indicating that there is single creep activation energy.

10.4.3. Reliability of Pb-Free Solder Joints in Comparison to Sn-Pb Eutectic Solder Joints

Reliability issues can manifest themselves in different forms of failure modes under different operating or testing conditions. The failure could be mechanical, such as fatigue failures: crack initiation and propagation; overstress failures, or it can be electrochemical, such as corrosion, electro-migration and dendrite growth [67]. Only mechanical reliability due to thermal CTE mismatch in service or in testing conditions is discussed in the following sections.

The thermo-mechanical reliability of Pb-free solder interconnects due to CTE mismatch in an electronic system (components, solder joints, and substrates) is determined by creep and fatigue interaction of the solder alloy [68]. Under typical conditions, Pb-free alloys are more creep resistant than the Sn-Pb alloy due to differences in microstructure (such as fine Ag_3Sn phases in the matrix and on the grain boundaries) [69]. In most applications, the Pb-free solder interconnects have been found to show better reliability than the

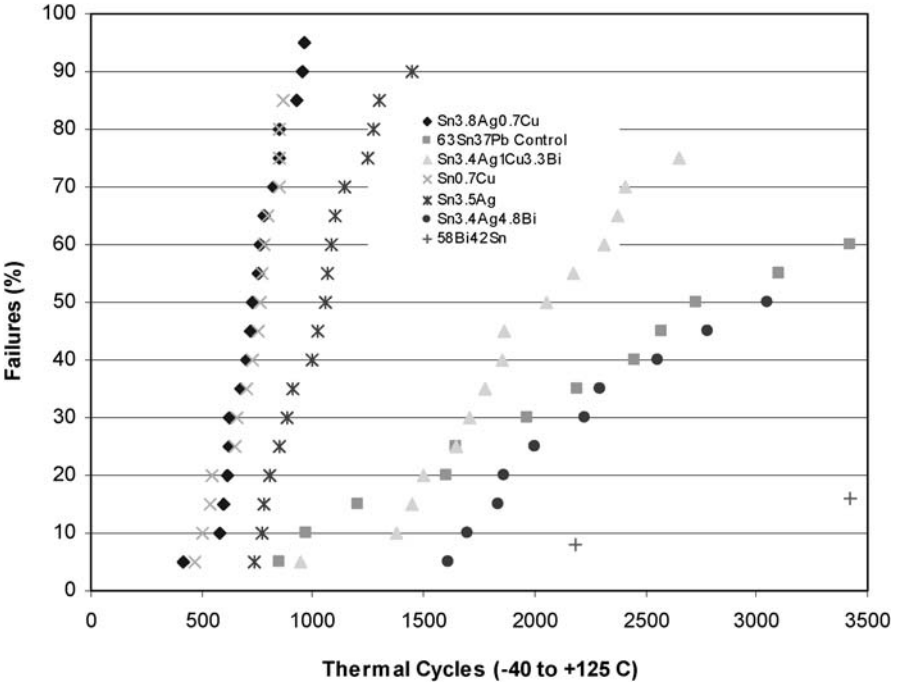

FIGURE 10.42. Thermal cycle reliability distribution curves for LCCC20 (−40°C to 120°C) [83].

Sn-Pb solder joints. However, this may not always be the case. The NCMS study has found that the ranking of Pb-free alloys in terms of reliability relative to Sn-Pb varies with the thermal cycle conditions and component types [70]. In most typical application conditions, the SAC solders are more reliable than the Sn-Pb solder. However, for very large components and components with a very large CTE mismatch with substrates, such as ceramic body components on FR4, and/or under very severe thermal cycling conditions, the Pb-free solder joints are indeed less reliable compared to the Sn-Pb solder joints, as evidenced in Figure 10.42, Figure 10.43 and Figure 10.44 [71–74]. Tests also show that for some leadless chip carriers and large size leadless chip resistors on FR4, and for Alloy 42 leaded components (such as TSOP 48), the fatigue life of Pb-free solder joints are significantly worse than those of the current Sn-Pb eutectic counterparts [69]. In the same NCMS study, it is found that for solder fatigue failure at 0°C to 100°C (10°C/min, 5-min dwell), the Pb-free Sn3.5Ag is similar to Sn-Pb eutectic, but at −55°C to 125°C (11°C/min, 20-min dwell), Sn-Pb eutectic shows much better fatigue life than Sn3.5Ag [52].

It is clear that a simple statement that Pb-free solders will generate more reliable joints could be misleading in certain design and application conditions, since these data above clearly indicate that the fatigue performance ranking of Pb-free alloys relative to Sn-Pb solder varies with thermal cycling conditions and component package types.

To understand the seemly confusing and contradictory reliability performance of Pb-free solder joints, one will need to examine carefully all extrinsic and intrinsic factors that most likely will determine the final fatigue life of a solder joint. Since Pb-free solders have quite different physical and mechanical properties from the current Sn-Pb eutectic solder, it is believed that the solder joint physical shape (geometry), stress and strain conditions, and materials resistance to deformation and fatigue fracture are also quite different for Pb-free

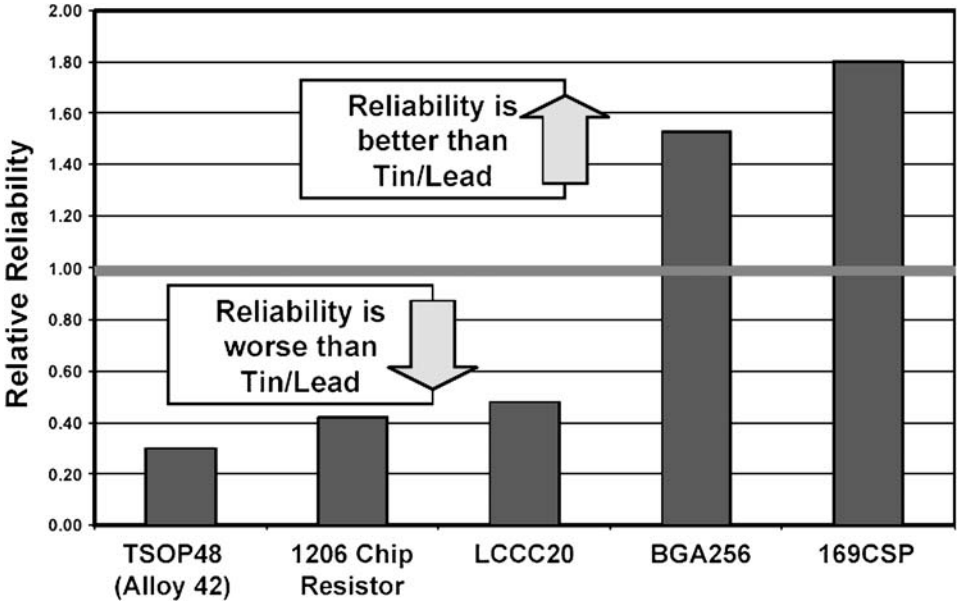

FIGURE 10.43. Comparison of reliability of Pb-free and Sn-Pb eutectic solder joints for different types of component packages [83].

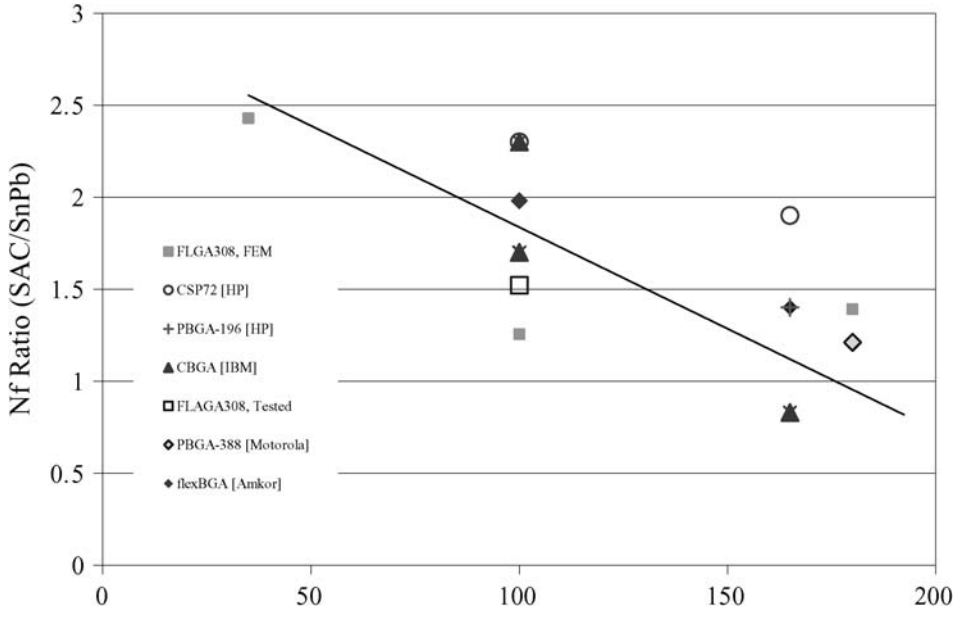

FIGURE 10.44. Fatigue life vs thermal cycling temperatures for a few different BGA packages [84,58,74].

and Sn-Pb eutectic solder joints, even with the same package type under a similar testing condition.

10.4.3.1. Factors That Affect Solder Joint Fatigue Life For any packaging technology, there are a few major extrinsic factors that affect thermal mechanical fatigue reliability of solder joints [75–77]. They include: board and package materials' mechanical and thermal properties, size and geometric dimensions; cyclic temperature profiles of the board and component, including the ramp rate, extreme temperatures, dwell times, etc; solder joint geometry (size, shape, height, etc.); environmental conditions: oxygen, nitrogen, or other reactive species. The intrinsic factors include solder alloy's chemical composition, microstructures, resistance to creep, monotonic and cyclic deformation, crack initiation and propagation, and material degradation sensitivity to complicated multi-axial stress–strain and environmental interactions. Failure of solder joints is usually a result of combined damages from fatigue, creep and environmental interaction. The above factors act together to determine what kind of stress and strain a solder joint will experience at a given time and temperature, and ultimately determine the life of the solder joints.

10.4.3.2. Loading Conditions of BGA Solder Balls The increased use of area-array technology in electronic packaging in recent years has given greater importance to the tasks of predicting and improving the thermal fatigue life of area array solder joints. These tasks typically involve the development of a "macro-model" of the entire assembly (component, substrate, and area array) to identify the critical joint and its end displacements; and a "micro-model" of the critical joint with the prescribed end displacements. The objective of the microanalysis is to determine the distribution of the stress, strain, and/or strain energy (or strain work) density in the critical joint. The output of the microanalysis may then be used as input to an appropriate fatigue life model.

In most cases, the maximum thermal mismatch at the critical joint can be expressed as:

$$\Delta u_{\max} = \beta_{sh} \Delta u_0, \tag{10.7}$$

where β_{sh} is the "shear correction factor" which will account for the combined effects of restraining factors that prevent the free thermal expansion, Δu_0, which is estimated to be:

$$\Delta u_0 = (\alpha_c \Delta T_c(t) - \alpha_s \Delta T_s(t)) \frac{\sqrt{L^2 + W^2}}{2}. \tag{10.8}$$

There also exists an out-of-plane displacement which will cause the board warpage and a tensile (or compression) stress on solder joints. In general, the critical joint (usually at the corner of a BGA array) will experience both shear Δu and z-axial Δw deformation [75,76]. The maximum z-directional (axial) displacement $\Delta w_{\max}$ can be related to the theoretical free thermal expansion Δu_0 as:

$$\Delta w_{\max} = \beta_z \Delta u_0, \tag{10.9}$$

where β_z is the z-axial correction factor, which is also dependent on all of the other restraining factors from PCB substrates and components, as well as solder joint shape and elastic or plastic characteristics, such as Young's modulus and Poisson ration, yielding strength and stress–strain hardening.

Exact analytic solutions for β_{sh} and β_z have been worked out and published for a few special cases of practical interest by the authors [75,76]. These correction factors are functions of the number of solder balls, solder joint geometry, pad size, Young's modulus and Poisson's ratio of solders. Figures 10.45 and 10.46 show the correction beta factors

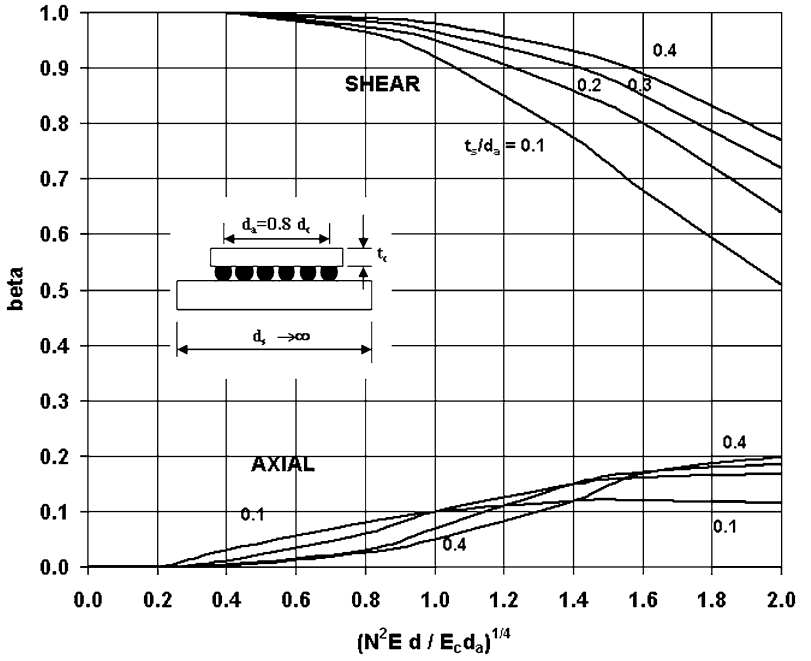

FIGURE 10.45. Shear and axial correction factors for a rigid-component assembly. Notice a positive (tensile) axial displacement [76].

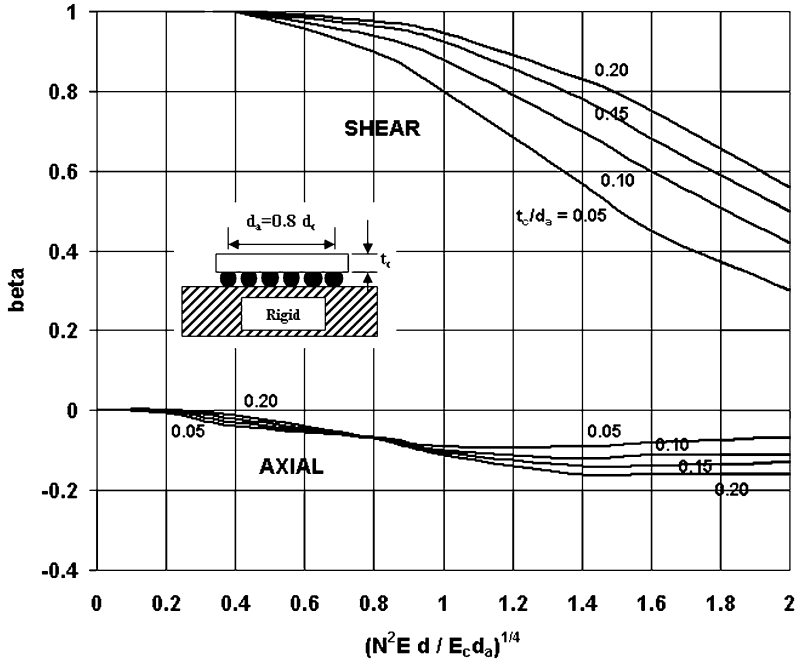

FIGURE 10.46. Shear and axial correction factors for a rigid substrate assembly. Notice a negative (compressive) axial displacement [76].

for two special cases where either component is rather rigid (Figure 10.45), such as in the case of a typical ceramic BGA or flip-chip package, or the PCB board substrate is rigid (Figure 10.46). It is clear that the analytical results establish a clear relationship between the correction factors and the physical parameters of the whole package and PCB system: (a) the dimensions, elastic and thermal properties of the component and substrate; (b) the mechanical properties of solder alloys (i.e., Young's modulus and Poisson's ratio); (c) the array size and population; and (d) the geometric parameters of the individual joints. For example, as shown in Figures 10.45 and 10.46, an increase in the number of solder balls, pad diameter and elastic modulus will increase the overall stiffness, thus causing a reduction of the shear beta factor, which effectively reduces the shear thermal deformation, and possibly, introduces a z-axial deformation, i.e., warping at the same time [76]. Changes in other geometric and mechanical parameters in substrates and components also have direct effects on the final shearing and tensile deformation on solder balls.

It is clear that the loading conditions on a BGA solder joint are mostly shearing and axial displacements, and are determined by geometric parameters and material mechanical properties of the entire assembly. The thermal cycling temperatures and profiles in service or testing will determine the loading amplitude and spectrum that a solder joint will experience with time. These shearing and axial displacements can be estimated fairly accurately. The result may be used as loading conditions (or boundary conditions) for solder joint life time assessment either based on first principles or based on time-dependent inelastic finite element analysis, should the creep and fatigue life models be available [54].

Shear strain on solder joints in service thermal and/or power cycling is generally the most damaging mechanical load to determine solder fatigue life and reliability. The shear strain $\gamma_{th}(t)$ is a function of the thermal mismatch, solder joint geometry and material elasto-plastic and creep constitutive relationships [54]. Depending on temperature and the magnitude of the total thermal mismatch, the strain at any given time is a combination of elastic, plastic and creep deformation. Furthermore, the solder strain and stress are not uniformly distributed in the solder joints; they are functions of location (x, y, z), temperature, time and pre-stress/strain history. A more accurate estimation of stress and strain on solder joints requires a complete understanding and mathematical modeling of solder alloy's plasticity and creep; and can be carried out only with a non-linear and time-dependent finite element modeling.

For a thermal cycle where ΔT_c and ΔT_s are given, the thermal fatigue life of the critical solder joints can be, based on the widely used modified Coffin-Mason equation, estimated as [77]:

$$N_f = \frac{1}{2}\left(\frac{\Delta\gamma_{in}}{\varepsilon_f}\right)^{\frac{1}{c}}, \tag{10.10}$$

where $\Delta\gamma_{in}$ is the inelastic strain range (for simplicity, it is roughly approximated as the average strain along a BGA solder ball); and c and ε_f are materials constants that are functions of thermal cycling temperatures and frequency [77]. As discussed above, all geometric and material parameters have their own contribution to the shear displacement, these effects are reflected in terms of the resultant shear strain, which then determines the final fatigue life.

Equations (10.7–10.10) and beta correction factors incorporate some of the most important factors of package design parameters, relevant material properties and service (or testing) conditions, into analytical expression for solder joint reliability assessment based

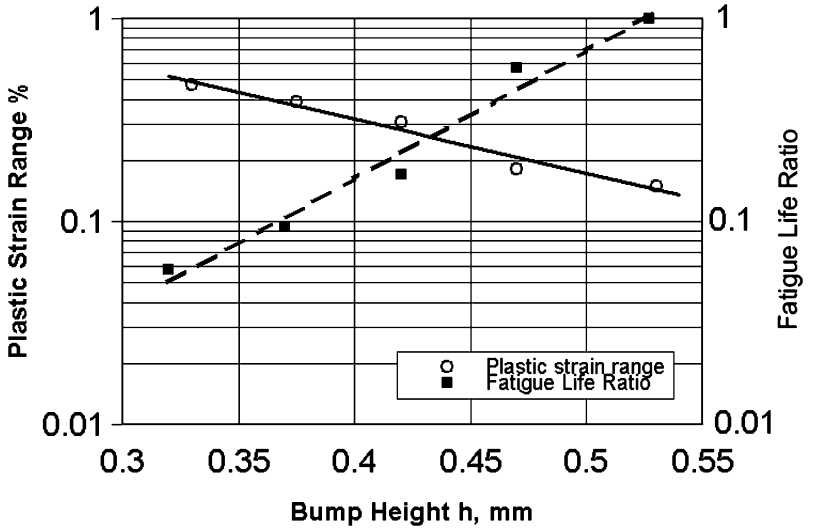

FIGURE 10.47. Solder ball height vs plastics stain and fatigue lives [78].

on simplified first principles. It is clear that the BGA balls' fatigue life is very sensitive to any slight change in solder joint height, solder volume, and CTEs for a given thermal cycle condition.

Figure 10.47 schematically shows solder joint bump height effect on estimated plastic strain range and thermal fatigue life of solder joints based on Sn-Pb eutectic solder [78]. It can be seen that when a solder joint's height is reduced from about 0.54 mm to 0.32 mm, the fatigue life can drop by more than 90%. It is apparent that the solder ball height is one of the most important and sensitive parameter to BGA reliability. In general, the solder ball cross-section along the height vary; the ball will assume different geometrical shape determined by the total solder volume, molten solder surface tension, component size and weight, as well as the soldering surface finishes. Stress and strain will concentrate around the smallest cross section area, leading to early fatigue crack initiation, and to a shorter fatigue life. Figure 10.48 shows the effects of solder ball geometry shape, height, and chip size on the fatigue life of Sn-Pb eutectic solder balls [79].

Since most published data on Pb-free solder reliability did not clearly state in what conditions the comparison to Sn-Pb solder is made (except for the thermal cycling profile), the difference in fatigue reliability performance is also likely due to the solder ball geometry and package materials because of different soldering temperatures and solder alloys' surface tension energy. Because Pb-free solders are generally stronger, the stiffening restraining effects on the maximum thermal shear displacement at the critical solder joint will be larger than that for the softer Sn-Pb eutectic solder. Likewise, the higher surface tension energy of Pb-free solder alloys could produce taller solder balls. Both factors would reduce the maximum thermal strain on Pb-free solder joints. Therefore, in theory, Pb-free solder joints can be more reliable than Sn-Pb eutectic joints for a similar package design due to these extrinsic factors, assuming both solders have a similar fatigue resistance. Elimination of the difference in these factors with well controlled test setup and samples could shed light on the real fatigue resistance of the alloys. Unfortunately, making identical solder joints out of two completely different metallurgical alloy systems are difficult. Therefore, an exact comparison and conclusive extrapolation about alloy performance based only on

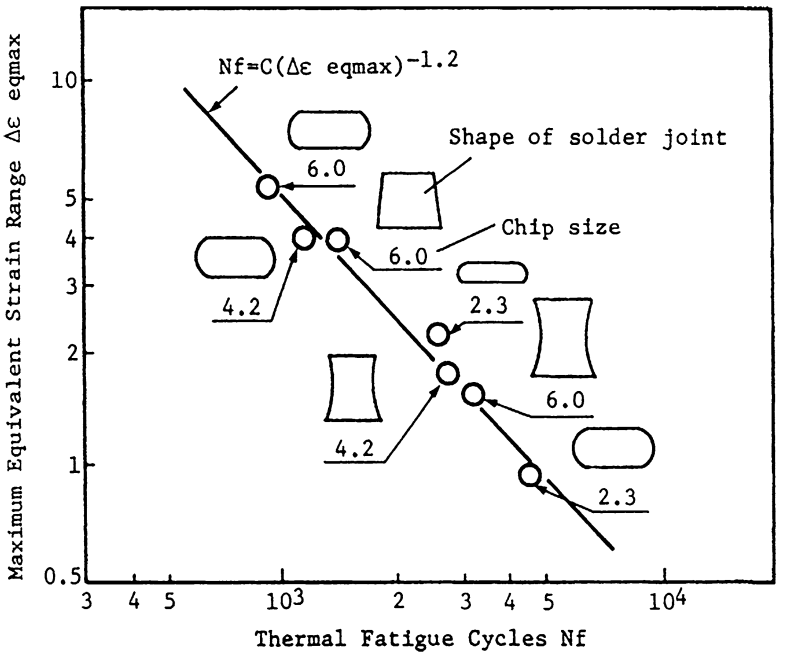

FIGURE 10.48. Effect of BGA ball geometry and chip size on fatigue life of Sn-Pb eutectic solder balls [79].

a few specific test configurations with Pb-free and Sn-Pb eutectic solder joints would not be viable.

10.4.3.3. Reliability of Pb-Free Alloys and Joints: Isothermal or Thermal Mechanical Fatigue? Since most factors indicate a longer fatigue lives of Pb-free solder balls for BGA applications, the discrepancy that in certain conditions Pb-free solder joints show a poor reliability compared to Sn-Pb eutectic points to some fundamental difference in thermal fatigue processes between Pb-free and Sn-Pb eutectic alloys.

It has been reported early by Soloman that temperature has no significant effect on low cycle fatigue (LCF) life of the Sn-Pb eutectic solders with strain control LCF tests up to 150°C [80]. Our previous study [66,81] for the modified eutectic alloy 62.5Sn-36.1Pb-1.4Ag, as shown in Figure 10.49, also proved this point, as well as with published data from M. Mukai [82], see Figure 10.50. However, temperature can have a significant effect on Pb-free alloys, such as 95Sn-5Ag, see Figure 10.51, which shows that an increase in temperature generally decreases the fatigue lives of the Sn5Ag alloy.

It is likely that temperature, strain rate, and stress levels may have significant effects on the thermal fatigue life of Pb-free alloys. Therefore, the simplified strain-range based fatigue life model, such as Equation (10.11), may not work well for Pb-free alloys. Most thermal fatigue life models are based on isothermal fatigue tests, where an isothermal equivalent temperature for a thermal cycle profile can be defined. For Pb-free alloys, however, not much experimental work has been conducted to establish a generally acceptable thermal fatigue life model. From the limited published and unpublished literature, fatigue life models based on stress–strain work density of hysteresis loops during thermal cycle tests, such as shown in Figure 10.52, clearly indicate that based on normalized creep strain energy density for thermal cycling tests, Sn-Pb eutectic solder has a cross-over with

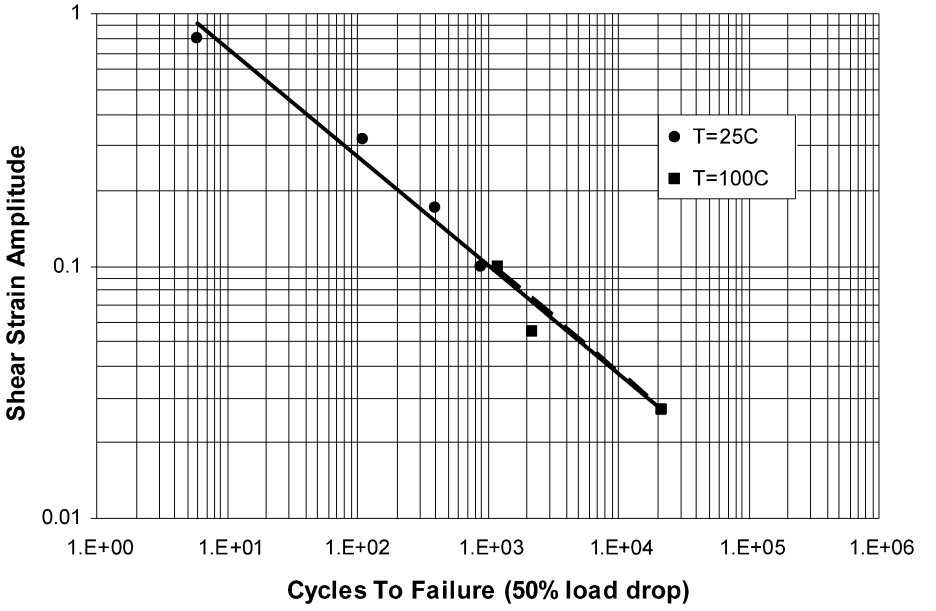

FIGURE 10.49. Temperature effects on isothermal low cycle fatigue life of Sn-Pb eutectic solder alloy [66,81].

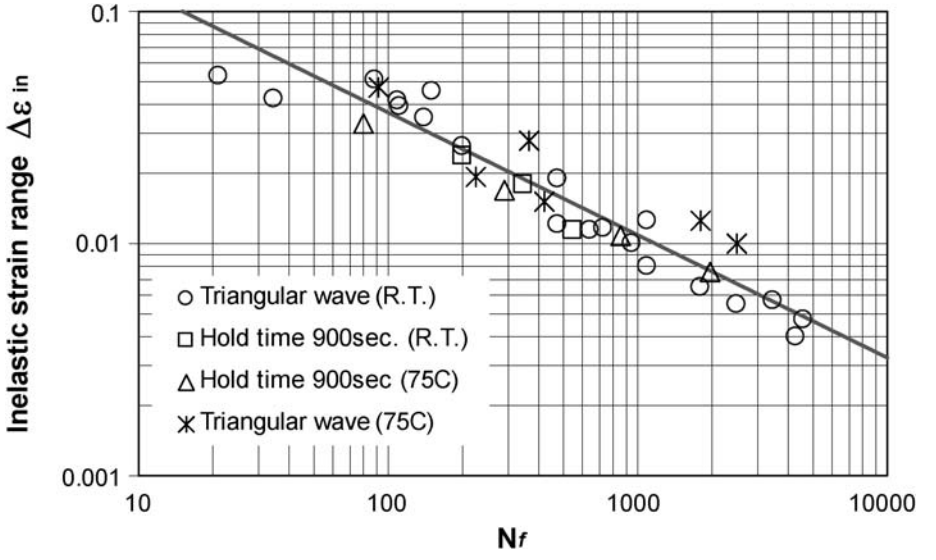

FIGURE 10.50. Fatigue life of eutectic solder vs cyclic inelastic (plastic) strain range at room temperature and 75°C with dwell times [83].

Pb-free alloys [83]. At higher stress–strain levels, the Sn-Pb eutectic solder has a superior fatigue resistance to Pb-free alloys; at lower or modest stress–strain levels, Pb-free alloys would outperform the Sn-Pb eutectic alloy. This is in a good agreement with above mentioned comparisons of BGA solder ball fatigue reliability, as shown in Figure 10.43 and Figure 10.44. Since for a relatively large component with a large thermal mismatch (such

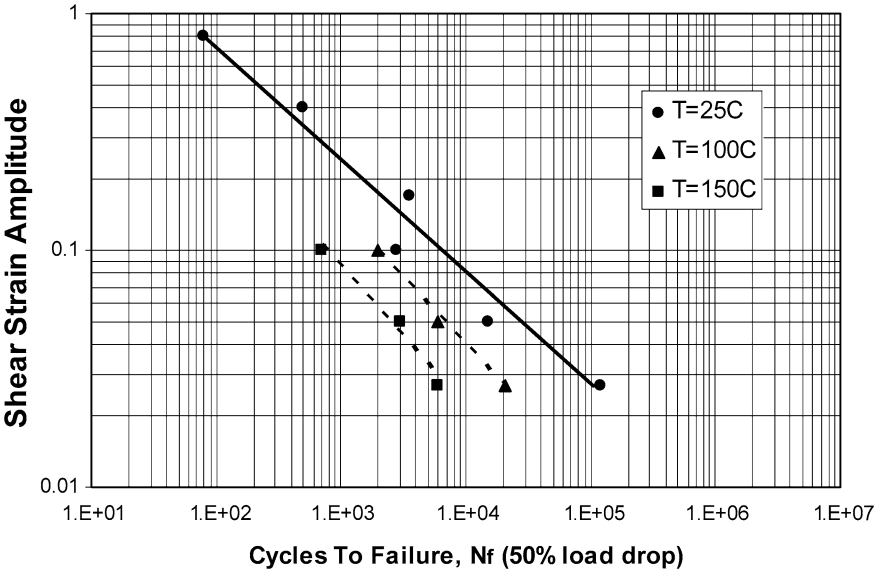

FIGURE 10.51. Temperature effects on isothermal low cycle fatigue life of a Pb-free solder alloy, 95Sn-5Ag [81,82].

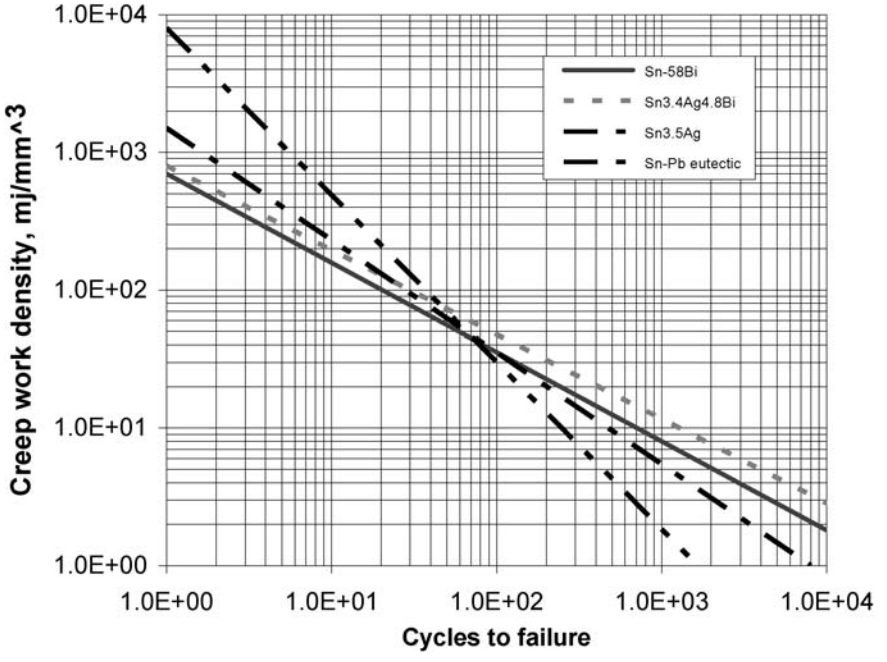

FIGURE 10.52. Thermal fatigue reliability comparisons of Pb-free and Sn-Pb alloys based on stress–strain work density in a thermal cycle [45,84].

as silicon and ceramic vs RF-4 substrate), a large thermal cycling temperature range will increase the stress–strain energy level, thus could result in lower thermal fatigue lives. For

ceramic BGA, the intrinsic large CTE mismatch and a near 1.0 shear beta factor could generate a condition where the thermal strain range for Pb-free alloys can be very high, thus result in a less favorable fatigue performance. Figure 10.44 clearly shows that with large thermal cycling, CBGA solder balls have lower fatigue lives than the Sn-Pb eutectic alloy joints. When the thermal cycle range is reduced, Pb-free solder balls then outperform the Sn-Pb solder joints.

From the above analyses and observation of most "discrepancy" for Pb-free alloys, it can be deduced that Pb-free alloys are much more sensitive to temperature in terms of reduction of creep resistance and isothermal low cycle fatigue performance. Therefore, the thermal fatigue life of a Pb-free solder joint will depend not only on the strain range, but also on the thermal cycle profile and strain rates, as well as the stress level. Thus, the energy-based fatigue life models, such as shown in Figure 10.52, would do a better job to characterize the fatigue reliability of Pb-free alloys and their joints.

This analysis shows that for more realistic service conditions encountered with most of the SMT leaded joints (such as QFP), when the lead stiffness is very low, the solder joint is most likely stressed well below its yielding point, and quite possibly, below the stress level where no significant time-dependent creep deformation may take place. Thus, solder alloys with a high creep resistance, such as SAC Pb-free alloys, will significantly improve SMT leaded joint reliability, as long as the lead stiffness and service temperature are not extremely high. On the contrary, for solders used in leadless interconnection or BGAs with large thermal mismatch and temperature swings, a low creep resistance and high ductility (such as the current soft Sn-Pb eutectic alloys) may prolong the solder joint fatigue life [54].

Since Pb-free solders are generally stronger and more creep resistant at the normal operational temperature range, a complaint lead design will lead to a better reliability of these leaded solder joints. However, if the leads are very stiff in geometry and/or of high modulus material, such as Alloy 42, the thermal mismatch will be transferred to the solder joints either with an instantaneous plastic deformation or through rather high rate creep. If the level of thermal strain is high due to CTE mismatch or a large thermal cycling temperature range, these leaded Pb-free solder joints could also show less favorable thermal fatigue life, as evidenced by TSOP 48-alloys 42 in Figure 10.43. It is clear that to fully utilize the good attributes of high yielding strength and high creep resistance of Pb-free alloys, stiff leads should be avoided.

10.4.3.4. Thermal Mechanical Fatigue Life Assessment In general, cyclic strain-range based fatigue life models, such as Equation (10.10), work well for isothermal low cycle fatigue of most engineering materials where material microstructure (except sub-cell dislocation structure) is relatively stable during the fatigue damage process. However, in most thermo-mechanical fatigue conditions, a simple strain range based fatigue life model may not work since it fails to take into consideration of the effects of peak stress and strain rate. Other fatigue life models, based on strain energy density, or models based on fatigue crack growth rate with help of non-linear fracture mechanics, may be needed for more accurate fatigue life assessment under thermo-mechanical conditions [84,85].

From early thermo-mechanical study of superalloys for aerospace applications, it has been learned that a stress–strain energy density fatigue life model could be a better fatigue failure criterion since it incorporates some effects of strain rates and temperatures. In general, a stress–strain energy-based fatigue life model can be expressed as:

$$N_f = c(W_{ss})^m, \tag{10.11}$$

where c and m are temperature-dependent material constants, which can be derived from isothermal low cycle fatigue tests at different temperatures; W_{ss} is the stress–strain hysteresis energy density. However, in practice, an accurate W_{ss} can not be estimated without establishing a complete temperature–stress–strain material constitutive relationship. The constitutive equation is necessary to model the effects of loading conditions and strain rates (or heating-up/cooling-down rates, dwell, etc.), which usually affect the peak stresses for a thermal cycling profile. In addition, inelastic strain (both plasticity and creep) can also be partitioned if necessary to use more advanced fatigue life models, such as strain-range partition or damage mechanics.

For Pb-free solders, there are not enough data to establish widely acceptable fatigue life models for the alloys themselves at this time. The models should be applicable for any testing or service condition, particularly in thermo-mechanical loading conditions encountered by solder joints. Well-controlled fatigue tests on Pb-free alloys with precise control of either stress and or strain are mostly conducted under isothermal conditions. To extend these fatigue life models to thermal cycle conditions where temperature and strain/stress changes take place simultaneously, will need much more investigation on Pb-free alloys. For solder joints, such as solder balls for BGA and leaded solder joints, which are mostly under multi-axial loading conditions with much more complicated non-uniform deformation and damage processes, thermal fatigue life assessment would require nonlinear and time dependent finite element analysis of stress/strain distribution. Doing so will also need much more study on Pb-free solder alloy's fundamental creep mechanisms and mathematical modeling.

10.5. GUIDELINES FOR PB-FREE SOLDERING AND IMPROVEMENT IN RELIABILITY

In summary, the mechanical loading, metallurgical structures and design parameters, as well as service (or test) conditions, all affect the reliability of Pb-free and Sn-Pb eutectic solder joints. Solder joint thermal deformation is determined not only by external environments, but also by the solder alloy itself and joint geometry. Comparison of solder joint reliability between Pb-free and Sn-Pb eutectic alloys does not always favor the high strength Pb-free alloys in all conditions. For isothermal low cycle fatigue with modest strain ranges, Pb-free alloys outperform Sn-Pb eutectic alloys. However under thermal mechanical conditions, Pb-free alloys show significant deterioration of reliability when large thermal strain and/or stress are encountered.

Pb-free solder alloys with a high creep resistance will significantly improve the reliability of BGA solder balls and compliant leaded solder joint as long as thermal mismatch and thermal cycling do not generate large inelastic deformation. On the contrary, for leadless joints, non-compliant leaded joints, and BGA with high CTE mismatch, a low creep resistance and high ductility Pb-free solder similar to the current Sn-Pb eutectic alloy would be more favorable.

REFERENCES

1. G. Humpston and D.M. Jacobson, Principles of Soldering, ASM International, Materials Park, OH, 2004.
2. J.F. Roeder, M.R. Notis, and H.J. Frost, in D.R. Frear, W.B. Jones, and K.R. Kinsma, Eds., Solder Mechanics, A State of the Art Assessment, TMS, 1991, p. 1.

3. E.E. de Kluizenaar, Soldering and Surf. Mount. Tech., 4, pp. 27–38 (1990).
4. Directive 2002/96/EC of the European Parliament and of the Council of 27 January 2003 on Waste Electrical and Electronic Equipment, Official Journal of the European Union, 13.2.2003, pp. L37/24–L37/38.
5. Directive 2002/95/EC of The European Parliament and of the Council of 27 January 2003 on the Restriction of the use of Certain Hazardous Substances in Electrical and Electronic Equipment, Official Journal of the European Union, 13.2.2003, pp. L37/19–L37/23.
6. Z. Mei and J.W. Morris, Jr., Journal of Electronic Materials (A.I.M.E. Metallurgical Society), 21, pp. 599–607 (1992).
7. N.-C. Lee, Lead-free soldering of chip-scale packages, Chip Scale Review, March/April, p. 42 (2000).
8. C.M.L. Wu, D.Q. Yu, C.M.T. Law, and L. Wang, The properties of Sn-9Zn lead-free solder alloys doped with trace rare earth elements, J. Electronic Mater., 31, pp. 921–927 (2002).
9. K.W. Moon, W.J. Boettinger, U.R. Kattner, F.S. Biancaniello, and C.A. Handwerker, J. Electronic Mater., 29, pp. 1122–1236 (2000).
10. C.-S. Oh, J.-H. Shim, B.-J. Lee, and D.N. Lee, J. Alloys and Compounds, 238, pp. 155–166 (1996).
11. J.H. Shim, C.-S. Oh, B.-J. Lee, and D.N. Lee, Z. Metallkde., 87, pp. 205–212 (1996).
12. K.S. Kim, S.H. Huh, and K. Suganuma, Mater. Sci. Eng. A, 333, p. 106 (2002).
13. J. Park, R. Kabade, C. Kim, T. Carper, S. Dunford, and V. Puligangla, J. Electronic Mater., 32, p. 1774 (2003).
14. B.P. Richards, C.L. Levoguer, C.P. Hunt, K. Nimmo, S. Peters, and P. Cusack, Lead-free soldering, an analysis of the current status of lead-free soldering, Department of Trade and Industry, UK, 2001.
15. J. Liang, N. Dariavach, P. Callahan, and D. Shangguan, Metallurgy and kinetics of liquid-solid interfacial reaction during lead-free soldering, Trans. Mater. (2005) (to be published).
16. F.G. Yost and A.D. Romig, Materials Research Society Symposium Proceedings, 108, pp. 385–390 (1988).
17. H. Wang and H. Conrad, Metall. Mater. Trans., 26A, pp. 495–469 (1995).
18. S.V. Sattiraju, R.W. Johnson, D.Z. Genc, and M.J. Bozack, Wetting performance vs. board finish and flux for several Pb-free solder alloys, PackCon 2000, October 2–3, Santa Clara, CA, 2000.
19. N. Dariavach, P. Callahan, J. Liang, and R. Fournelle, A study of intermetallic growth kinetics for Sn-Ag, Sn-Cu and Sn-Ag-Cu lead-free solders on Cu, Ni and Fe-42Ni substrates, TMS 05, 2005.
20. K. Suganuma and G. Nakamura, J. Japan Inst. Metals., C59, p. 1299 (1995).
21. M. Schaefer, W. Laub, R.A. Fournelle, and J. Liang, in R.K. Mahidhara, et al., Eds., Design and Reliability of Solders and Solder Interconnects, TMS, Warrendale, PA, 1997, p. 247.
22. S. Chada, R.A. Fournelle, W. Laub, and D. Shangguan, J. Electronic Mater., 29, p. 1214 (2000).
23. S. Chada, W. Laub, R.A. Fournelle, and D. Shangguan, J. Electronic Mater., 28, p. 1194 (1999).
24. H.K. Kim and K.N. Tu, Phys. Rev. B, 53(23), p. 16027 (1996).
25. M. Schaefer, R.A. Fournelle, and J. Liang, J. Electronic Mater., 27, p. 1167 (1998).
26. R.A. Gagliano and M.E. Fine, J. Electronic Mater., 32, p. 1441 (2003).
27. ASM Handbook, Vol. 8, Metallography, Structures and Phase Diagrams, 8th Edition, ASM, 1973.
28. J. Oliver, M. Nylen, O. Rod, and C. Markou, Fatigue properties of Sn3.5Ag0.7Cu solder joints and effects of Pb-contamination, Proceedings of SMTA International Conference, Chicago, IL, Sept. 2002.
29. R. Gordon, S. Marr, and D. Shangguan, Evaluation of immersion silver PWB finish for automotive electronics, Proceedings of SMTA International Conference, Chicago, September 2000, pp. 583–591.
30. M. Arra, D. Shangguan, and D. Xie, Wetting of fresh and aged lead-free PCB surface finishes by Sn/Ag/Cu solder, Proceedings of APEX 2003, Anaheim, CA, March 2003, pp. S209–2-1/5.
31. M. Arra, D. Shangguan, J. Sundelin, T. Lepistö, and E. Ristolainen, Aging mechanisms of immersion tin and silver PCB surface finishes, Proceedings of the 3rd IPC/JEDEC Annual Conference on Lead-Free Electronic Assemblies and Components, 2003, pp. 170–179.
32. M. Arra, D. Shangguan, D. Xie, J. Sundelin, T. Lepistö, and E. Ristolainen, Study of immersion silver and tin PCB surface finishes in lead-free solder applications, Proceedings of Soldertec/IPC International Lead-free Conference, Brussels, Belgium, 11–12 June 2003, pp. 423–446.
33. M. Arra, D. Geiger, D. Shangguan, S. Yi, F. Grebenstein, H. Fockenberger, K.H. Kerk, and H. Wong, Performance evaluation of lead-free solder paste, Proceedings of SMTA Conference, Chicago, IL, Oct. 2001, pp. 850–857.
34. M. Arra, D. Shangguan, E. Ristolainen, and T. Lepisto, Solder balling of lead-free solder paste, J. Electronic Mater., 31(11), pp. 1130–1138 (2002).
35. M. Arra, D. Shangguan, E. Ristolainen, and T. Lepistö, Effect of reflow profile on wetting and intermetallic formation between Sn/Ag/Cu solder, components and printed circuit boards, Soldering and Surf. Mount. Tech., 14(2), pp. 18–25 (2002).

36. M. Arra, D. Shangguan, S. Yi, H. Fockenberger, and R. Thalhammer, Development of lead-free wave soldering processes, IEEE CPMT Transactions on Electronics Packaging Manufacturing, 25(4), pp. 289–299 (2002). Also, Proceedings of APEX 2002, San Diego, CA, Jan. 2002, pp. 4(1)–4(10).
37. J. Lau, D. Shangguan, W. Dauksher, D. Khoo, G. Fan, W. Loong-Fee, and M. Sanciaume, Lead-free wave-soldering and reliability of a light-emitting diode (LED) display, Proceedings of Soldertec/IPC International Lead-free Conference, Brussels, Belgium, 11–12 June 2003, pp. 116–124.
38. I. Amato, Tin whiskers: the next Y2K problems? January, 10, FORTUNE, 2005, p. 27.
39. P.J.T.L. Oberndorff, M. Dittes, and L. Petit, Intermetallic formation in relation to tin whiskers, Proceedings of IPC/SolderTec, International Conference on Lead Free Electronics, Brussels, Belgium, June 11–12, p. 171.
40. J. Liang, X. Li, Z. Xu, and D. Shangguan, Nano-indentation study on whisker formation on tin plated component leads, IPC/JEDEC 8th International Conference on Lead-free Electronic Components and Assemblies, San Jose, CA, April 18–20, 2005.
41. EMC/Brown, Stress Evolution and Whisker Formation in Cn-Sn Bimetallic Layers, June 1, 2004.
42. JEDEC, Qualification requirements for tin whisker mitigation practices of component lead finishes, Draft, Nov., 2004.
43. D. Geiger, D. Shangguan, and S. Yi, Thermal study of lead-free reflow soldering processes, Proceedings of the 3rd IPC/JEDEC Annual Conference on Lead-Free Electronic Assemblies and Components, 2003, pp. 95–98.
44. D. Geiger, J. Yu, and D. Shangguan, Development of assembly and rework processes for large and complex PCBs using lead-free solder, Proceedings of APEX 2004.
45. D. Shangguan, Supply chain impact of lead-free soldering, Proceedings of the 10th Annual Pan Pacific Microelectronics Symposium, Kauai, Hawaii, January 2005.
46. D. Shangguan, A holistic approach to lead-free transition and environmental compliance, Proceedings of SMTA 2004, Chicago, IL, 2004.
47. J.H. Lau and D. Rice, Solder joint fatigue in surface mount technology: state of the art, Solid State Technology, 28(October), pp. 91–104 (1985).
48. J.H. Lau, Thermal stress analysis of SMT PQFP packages and interconnections, ASME Transactions, Journal of Electronic Packaging, 111(March), pp. 2–8 (1989).
49. J.H. Lau, G. Harkins, D. Rice, J. Kral, and B. Wells, Experimental and statistical analyses of surface mount technology PLCC solder joint reliability, IEEE Transactions on Reliability, 37(5), pp. 524–530 (1988).
50. R.R. Tummala, Fundamentals of Microsystems Packaging, McGraw-Hill, New York, NY, 2001.
51. J. Lau, N. Hoo, R. Horsley, J. Smetana, D. Shangguan, W. Dauksher, D. Love, I. Menis, and Sullivan, Reliability testing and data analysis of high-density packages' lead-free solder joints, Soldering and Surf. Mount. Tech., 16(2), pp. 46–68 (2004). Also, Proceedings of APEX 2003, Anaheim, CA, March 2003, pp. S42-3-1/24.
52. NCMS Report 0401RE96, Lead-Free Solder Project, Final Report, National Center for Manufacturing Sciences, August 1997.
53. J. Hwang, SMT March 2001, 2001, p. 70.
54. J. Liang, et al., Advances in Electronic Packaging, 1997, AMSE InterPack'97, ASME, 1997, pp. 1583–1592.
55. D.S. Stone and M.M. Rashid, in D.R. Frear, S.N. Burchett, H.S. Morgan, and J.H. Lau, Eds., The Mechanics of Solder Alloy Interconnects, Van Nostrand Reinhold, New York, 1994, pp. 87–157.
56. D. Shangguan, Study of compatibility for lead free solder PCB assembly, Proceedings of International Conference on Lead-Free Electronics, SolderTec, Brussels, June, 2003, pp. 297–308.
57. J. Clech, Proceedings of IPC/SMEMA APEX 2004 Conference, Anaheim, CA, Feb., 21–26, 2004.
58. J. Lau, N. Hoo, R. Horsley, J. Smetana, D. Shangguan, W. Dauksher, D. Love, I. Menis, and B. Sullivan, Reliability testing and data analysis of high-density packages' lead-free solder joints, Proceedings of APEX 2003, Anaheim, CA, March 2003.
59. D.R. Frear, S.N. Burchett, and H.S. Morgan, Introduction: the mechanics of solder alloy interconnection, in D.R. Frear, S.N. Burchett, H.S. Morgan, and J.H. Lau, Eds., The Mechanics of Solder Alloy Interconnects, Van Nostrand Reinhold, New York, 1994, pp. 1–6.
60. J. Liang, N. Dariavach, and D. Shangguan, Deformation behavior of solder alloys under variable strain rate shearing and creep conditions, IEEE International Symposium and Exhibition on Advanced Packaging Materials, Irvine, CA, USA, March 16–18, 2005.
61. J. Liang, N. Dariavach, P. Callahan, G. Barr, D. Shangguan, and C. Li, Deformation and fatigue fracture of solder alloys under complicated load conditions, InterPACK '05, The ASME/Pacific Rim Technical Conference and Exhibition on Integration and Packaging of MEMS, NEMS, and Electronic Systems, San Francisco, CA, Westin St. Francis Hotel, July 17–22, 2005.

62. E. Krempl, The role of servocontrolled testing in the development of theory of viscoplasticity based on total strain and overstress, in R.W. Rohde and J.C. Swearenger, Eds., Mechanical Testing for Deformation Model Development, ASTM STP 765, ASTM, 1982, pp. 5–28.
63. J.H. Gittus, Creep, Viscoelasticity and Creep Fracture in Solids, John Wiley & Son Inc., 1975.
64. E. Orowan, J. West Scotl. Iron Steel Inst., 54, p. 45 (1946).
65. H. Riedel, Fracture at High Temperatures, Springer-Verlag, 1986.
66. J. Liang, N. Gollhardt, P.S. Lee, S.A Schroeder, and W.L. Morris, A study of fatigue and creep behavior of four high temperature solders, Fatigue Fract. Engng Mater. Struct., 19, pp. 1401–1409 (1996).
67. J. Liang, N. Dariavach, and S. Downs, Load conditions and reliability of Pb-free solder alloys and solder joints, IPC/Soldertec Global 2nd International Conference on Lead Free Electronics, Towards Implementation of the RoHS Directive, Amsterdam, June 21–23, 2004.
68. W. Ren, M. Lu, S. Liu, and D. Shangguan, Thermal mechanical property testing of lead-free solder joints, Soldering and Surf. Mount. Tech., 9(3), pp. 37–40 (1997).
69. T.A. Woodrow, Reliability and leachate testing of lead-free solder joints, Proceedings of the International Conference on Lead-Free Components and Assemblies, San Jose, CA, May 1–2, 2002, pp. 116–125.
70. NCMS Report 0401RE96, Lead-Free Solder Project, Final Report, National Center for Manufacturing Sciences, August 1997.
71. D. Shangguan, Study of compatibility for lead free solder PCB assembly, Proceedings of International Conference on Lead-Free Electronics, SolderTec, Brussels, June, 2003, pp. 297–308.
72. J. Lau, N. Hoo, R. Horsley, J. Smetana, D. Shangguan, W. Dauksher, D. Love, I. Menis, and B. Sullivan, Reliability testing and data analysis of high-density packages' lead-free solder joints, Proceedings of APEX 2003, Anaheim, CA, March 2003.
73. T.A. Woodrow, Reliability and leachate testing of lead-free solder joints, Proceedings of the International Conference on Lead-Free Components and Assemblies, San Jose, CA, May 1–2, 2002, pp. 116–125.
74. D. Xie, M. Arra, H. Phan, D. Shangguan, D. Geiger, and S. Yi, Life prediction of leadfree solder joints for handheld products, Proceedings of the Telecomm Hardware Solutions Conference & Exhibition, SMTA/IMAPS, Legacy Park, TX, May 2002, pp. 83–88.
75. S. Heinrich, J. Liang, and P.S. Lee, Advances in Electronic Packaging 1999, ASME InterPack'99, ASME, 1999, pp. 43–53.
76. S.M. Heinrich, P.S. Lee, and J. Liang, Analytical expressions for shear and axial joint deformations in area-array assemblies due to CTE mismatch, Proceedings, 2002 ASME International Mechanical Engineering Congress and Exposition, Vol. 2, Paper No. IMECE2002-39636, 13 pp., New Orleans, LA, November 17–22, 2002.
77. W. Engelmaier, in J.H. Lau, Ed., Solder Joint Reliability—Theory and Applications, Van Nostrand Reinhold, New York, 1991, pp. 545–587.
78. M. Kitano and M. Honda, in Advances in Electronic Packaging, 1997, AMSE InterPack'97, ASME, 1997, pp. 1407–1412.
79. R. Satoh, K. Arakawa, M. Harada, and K. Matsui, IEEE Trans. on CHMT, 14, pp. 224–232 (1991).
80. H.D. Solomon, in H.D. Solomon, G.R. Halford, L.R. Kaisand, and B.N. Leis, Eds., Low Cycle Fatigue, ASTM STP 942, ASTM, 1988, pp. 342–370.
81. J. Liang, N. Gollhardt, P.S. Lee, S.A. Schroeder, and W.L. Morris, in J.C. Suhling, Ed., Applications of Experimental Mechanics to Electronic Packaging, ASME, 1995, pp. 1–9.
82. M. Mukai, et al., Fatigue life estimation of solder joints in SMT-PGA packages, Journal of Electronic Packaging, ASME, 120(June), p. 207 (1998).
83. Q. Zhang, P. Friesen, and A. Dasgupta, Risk assessment & accelerated qualification, of Pb-free electronics, CALCE Project C03-05, 2003.
84. J. Liang, and R.M. Pelloux, Chin J. Met. Sci. & Technol., 5, pp. 1–12 (1989).
85. J.D. Morrow, Cyclic plastic strain energy and fatigue of metals, ASTM STP 378, ASTM, pp. 45–87 (1964).